Computer Methods in Applied Mechanics and Engineering 459 (2026) 119034

Contents lists available at ScienceDirect

Comput. Methods Appl. Mech. Engrg.

journal homepage: www.elsevier.com/locate/cma

Unsupervised full-field Bayesian inference of orthotropic hyperelasticity from a single biaxial test: a myocardial case study

Rogier P. Krijnen [a], Akshay Joshi [b], Siddhant Kumar [c], Mathias Peirlinck [a,*]

[a] Department of BioMechanical Engineering, Delft University of Technology, Netherlands
[b] Department of Mechanical Engineering, Indian Institute of Science, Bengaluru, India
[c] Department of Materials Science and Engineering, Delft University of Technology, Netherlands

ARTICLE INFO

Dataset link: github.com/peirlincklab

Keywords:
Material model inference
Full-field kinematics
Uncertainty quantification
Anisotropic hyperelasticity
Experimental tissue testing
Bayesian inference

ABSTRACT

Cardiac muscle tissue exhibits highly non-linear hyperelastic and orthotropic material behavior during passive deformation. Traditional constitutive identification protocols therefore combine multiple loading modes and typically require multiple specimens and substantial handling. In soft living tissues, such protocols are challenged by inter- and intra-sample variability and by manipulation-induced alterations of mechanical response, which can bias inverse calibration. In this work we exploit spatially heterogeneous full-field kinematics as an information-rich alternative to multimodal testing. We recast EUCLID, an unsupervised method for the automated discovery of constitutive models, towards Bayesian parameter inference for highly nonlinear, orthotropic constitutive models. Using synthetic myocardial tissue slabs, we demonstrate that a single heterogeneous biaxial experiment, combined with sparse reaction-force measurements, enables robust recovery of Holzapfel–Ogden parameters with quantified uncertainty, across multiple noise levels. The inferred responses agree closely with ground-truth simulations and yield credible intervals that reflect the impact of measurement noise on orthotropic material model inference. Our work supports single-shot, uncertainty-aware characterization of nonlinear orthotropic material models from a single biaxial test, reducing sample demand and experimental manipulation.

1. Introduction

Soft biological tissues exhibit complex mechanical responses due to their fibrous, anisotropic microstructure. Accurately characterizing this behavior is essential for constructing predictive constitutive models that support simulation-driven design, diagnostics, and treatment planning [1,2]. However, unlike engineered materials, soft tissues are subject to considerable biological variability, both within a patient, across a patient cohort, and across experimental studies [3–7]. This intra- and inter-sample variability is even more pronounced in the myocardium, where strong spatial gradients in myofiber orientation and laminar architecture govern regional mechanical function [8,9]. Here, we *investigate the impact that the underlying microstructural organization variability has on the mechanical behavior of a single sample.*

Traditional approaches to constitutive modeling of such tissues typically rely on multiple mechanical tests across different deformation modes including uniaxial tension or compression, biaxial tension, or shear testing [10–12]. These protocols often require combining data from different specimens and, as such, ignore and smooth out intrinsic intra- and inter-sample variability into an average response [13]. Moreover, these protocols involve strong assumptions, such as spatially homogeneous stress and strain fields

* Corresponding author.
E-mail address: mplab-me@tudelft.nl (M. Peirlinck).

https://doi.org/10.1016/j.cma.2026.119034
Received 14 January 2026; Received in revised form 25 April 2026; Accepted 25 April 2026
Available online 20 May 2026

within the region of interest [14–16]. Such assumptions are problematic for living tissues, where spatial heterogeneity is the norm, and the mechanical response may depend on subtle differences in fiber orientation, geometry, inter-sample variable stiffness, or mounting. In addition, invasive sample manipulations, such as cutting, clamping, and gluing, can alter the intrinsic mechanical behavior that these tests seek to measure [17–19].

These challenges have prompted the development of single-sample, single-experiment methodologies that aim to infer full constitutive behavior from a single loading protocol. This shift has been enabled by advances in full-field deformation measurements, such as digital image correlation and imaging-based 3D kinematics [20–22]. When applied to samples undergoing spatially heterogeneous deformation, such data enable the inference of multiple material parameters simultaneously, reducing the need for multiple loading modes. Indeed, unsupervised identification techniques, such as the virtual fields method (VFM) [23,24], finite element model updating (FEMU) [25–27], variational systems identification [20], the equilibrium gap method (EGM) [28,29], and EUCLID [30–33], demonstrate that heterogeneous strain states, once seen as a nuisance, can be leveraged as rich sources of information, obviating the need for homogenizing assumptions. In this study, we *assess the extent to which a simple biaxial tensile testing protocol on a single myocardial tissue slab can support identification of the underlying orthotropic behavior*.

Yet, a key limitation persists in most current workflows: the lack of uncertainty quantification. Material parameters are frequently reported as point estimates, with little accounting for the inherent measurement noise or biological variability. In the context of myocardial modeling, where even adjacent samples can differ markedly in stiffness and fiber orientation [10,34], such deterministic inference may be misleading [35]. Recent work has begun to address this gap through Bayesian approaches to inverse modeling, which offer not only best-fit estimates but also posterior distributions reflecting uncertainty in data and model form [32,36–41]. Within the unsupervised setting, Bayesian-EUCLID forms an interesting contribution towards the inference of myocardial tissue behavior from full-field displacement fields and force measurements. In prior work, Joshi et al. demonstrated the feasibility of using Gibbs sampling for full-field inference in two-dimensional problems [32], where the material response could be inferred from a linear system of equations for the unknown material parameters in a rich constitutive feature library.

In contrast, the setting of this study involves two distinct and compounding challenges. First, the underlying constitutive models are highly nonlinear [14,16,42], with strongly cross-correlated parameters [15,43] that give rise to complex posterior landscapes. Second, we transition to three-dimensional full-field data. While the latter provides richer information, it also substantially increases the computational cost of evaluating the likelihood function. These factors independently and jointly limit the practical utility of Markov Chain Monte Carlo (MCMC) methods, including Gibbs sampling, due to the high cost of repeated likelihood evaluations and the poor mixing behavior in high-dimensional, correlated spaces. These limitations *motivate adapting the Bayesian EUCLID framework with more scalable inference strategies, such as Stochastic Variational Inference (SVI)*, which approximates posterior distributions through optimization rather than sampling, enabling *tractable inference in settings with both complex models and large data volumes*.

Towards these goals, this study presents an extensive numerical study using an unsupervised, full-field, Bayesian framework for the inference of orthotropic hyperelastic material parameters from a single synthetic heterogeneous biaxial tensile test. Our approach builds on the Bayesian-EUCLID framework [32], extended via SVI to capture parametric uncertainty in a highly nonlinear, a priori chosen constitutive model form. The myocardium is modeled using the well-established Holzapfel–Ogden constitutive law [14,44], and heterogeneity in the deformation field is introduced either through microstructural variation (i.e., intrinsic fiber-sheet-interlaminar architectural heterogeneity), geometric tissue sample modification, or both. We demonstrate that the spatial richness of the synthetic heterogeneous displacement field combined with reaction force data enables robust parameter inference with uncertainty quantification from a single test. We additionally validate the inferred material models using unseen invariant values and assess sensitivity to displacement noise. Finally, we restrict attention to a controlled numerical setting, which allows us to isolate the effects of noise, heterogeneity, and model nonlinearity on inference performance, factors that are typically confounded in experimental data. *Overall, this work highlights the potential of full-field, unsupervised, and uncertainty-aware approaches to redefine how we efficiently characterize complex biological tissues, taking into account minimal tissue availability and minimizing tissue manipulation.*

2. Unsupervised stochastic variational constitutive parameter inference

Conventional approaches for characterizing myocardial material behavior typically rely on spatially averaged measurements and simplifying assumptions of spatially homogeneous microstructural organization. However, this intrinsic homogenization obscures the spatial heterogeneity present within a tissue sample. To address this, we infer the constitutive parameter vector in an unsupervised setting from experimentally accessible data: (i) global reaction forces, (ii) full-field deformation, and (iii) microstructural organization across the slab. In this work, we assume digital volume correlation (DVC) data derived from concomitant through-thickness imaging, such as ultrasound [45], Magnetic Resonance Imaging [46], or X-ray Imaging [47] to obtain three-dimensional deformation fields. In parallel, microstructural maps can be obtained via SHG or micro-CT [12,48,49]. Among established inverse constitutive identification strategies such as FEMU, VFM, and EGM, we adopt an FE-based weak-form residual formulation building on EUCLID [30,32]. In contrast to FEMU, which requires repeated finite element solves for each parameter update and load step, we evaluate the weak form of momentum balance directly from the measured displacement field (see Section 2.1), thereby avoiding repeated forward equilibrium solves and suggesting an expected computational advantage, particularly for high-dimensional or highly nonlinear problems. The present formulation is related in spirit to both VFM and EGM as full-field alternatives to FEMU. It differs from classical VFM in that it uses the Bubnov–Galerkin finite-element test space induced by the reconstruction mesh rather than a reduced set of hand-crafted or parameter-specific virtual fields, and from EGM in that it relies on the weak rather than strong form of momentum balance, thereby reducing sensitivity to noise in the measured kinematics. Building on this residual formulation, we extend the method to a fully three-dimensional setting with nonlinear orthotropic materials and recast the classic deterministic

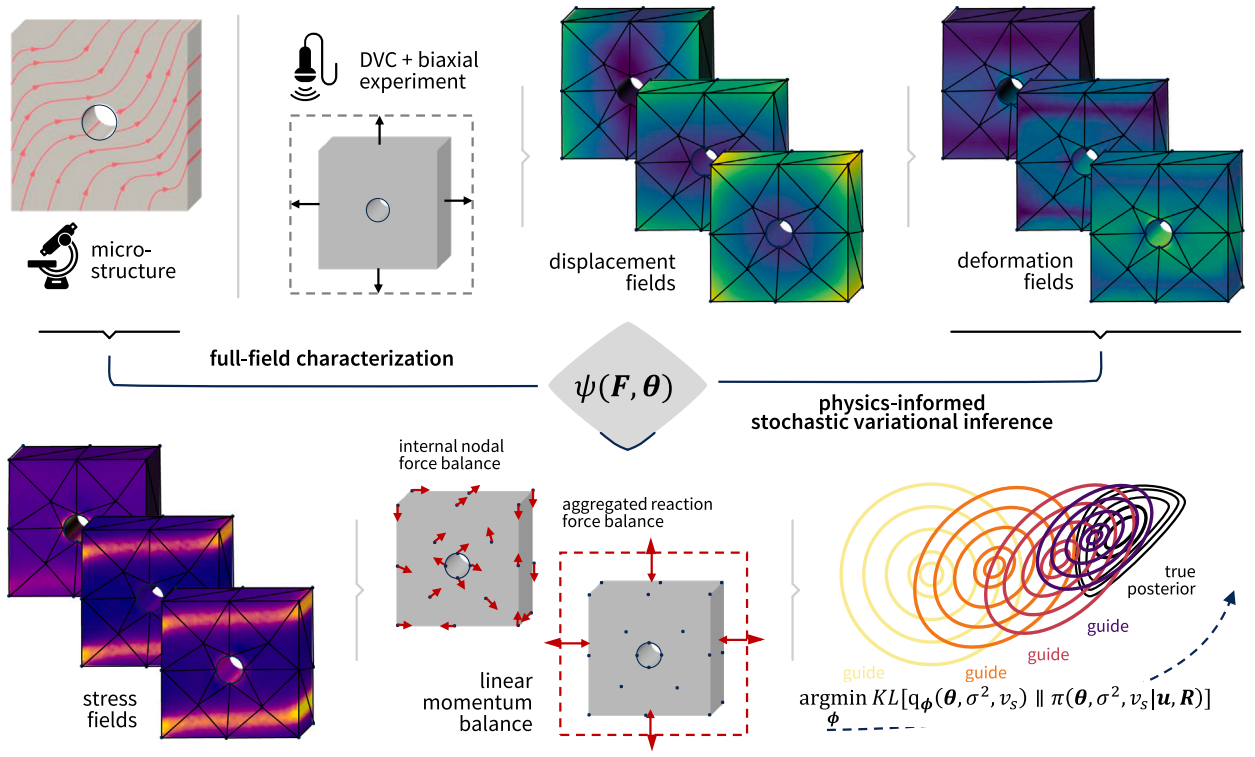

Fig. 1. Schematic overview of our unsupervised full-field stochastic variational inference framework for orthotropic hyperelastic tissue behavior. Quantification of the tissue's microstructural organization, such as spatially varying fiber orientations, provides essential architectural information across the sample domain. In parallel, point-wise measurements of displacements $\boldsymbol{u}$ and reaction forces $\boldsymbol{R}$ are acquired under quasi-static biaxial loading using digital volume correlation. The sample geometry is discretized into a finite element mesh, enabling reconstruction of continuous deformation fields $\boldsymbol{F}$ from the measured data. A nonlinear orthotropic constitutive model ψ, parameterized by a set of cross correlated material parameters $\boldsymbol{\theta}$, serves as the mechanistic basis for inference. Given the reconstructed deformation and microstructural organization fields, the model predicts stress responses at the element level, which are used to compute internal and external nodal forces. Residuals are formulated through the weak form of the conservation of linear momentum, minimized pointwise for unconstrained degrees of freedom and in aggregate at boundaries with known reaction forces. The inverse problem is cast as a stochastic variational inference task, where a variational guide distribution $q_{\boldsymbol{\Phi}}(\boldsymbol{\theta},\sigma^2,\upsilon_s)$ approximates the true posterior $\pi\left(\boldsymbol{\theta},\sigma^2,\upsilon_s \mid \boldsymbol{u},\boldsymbol{R}\right)$ by minimizing the Kullback–Leibler divergence $\mathrm{KL}\left(q_{\boldsymbol{\Phi}}\left(\boldsymbol{\theta},\sigma^2,\upsilon_s\right) \parallel \pi\left(\boldsymbol{\theta},\sigma^2,\upsilon_s \mid \boldsymbol{u},\boldsymbol{R}\right)\right)$. Our physics-informed constitutive inference framework enables efficient and scalable inference from complex high dimensional full-field deformation datasets, accommodating nonlinear material behaviors and cross-correlated parameter effects.

parameter optimization into an unsupervised Bayesian inference problem. Leveraging Stochastic Variational Inference (SVI), we infer posterior distributions over the constitutive parameters while accounting for uncertainty in the equilibrium residuals induced by noisy displacement and reaction-force measurements. We identify orthotropic hyperelastic parameters from a single biaxial test; the overall workflow is summarized in Fig. 1 and detailed in Section 2.2.

2.1. EUCLID preliminaries

We first define the kinematic and force data available from a single experiment, and then derive the equilibrium residuals that underpin deterministic parameter identification. Consider a myocardial tissue specimen undergoing quasi-static deformation in a three-dimensional reference domain $\Omega \subset \mathbb{R}^3$. Depending on the tissue slab's extraction orientation protocol (see Section 3), the underlying myocardial microstructure variation induces diverse and heterogeneous strain states. In this work, this heterogeneity enters through spatially varying structural fields, while the constitutive parameter vector $\boldsymbol{\theta}$ is assumed to be spatially homogeneous and thus constant over Ω. This separation attributes spatial variability to the structural inputs while keeping the inverse problem focused on a single parameter vector. Optionally, additional tissue manipulations, e.g., cutting a hole in the tissue slab or local cardiac ablation, can further promote a highly heterogeneous deformation state during biaxial tensile testing.

Boundary conditions are applied such that Dirichlet conditions are enforced on $\partial\Omega_u \subset \partial\Omega$ and Neumann conditions on the remainder, $\partial\Omega_t = \partial\Omega \setminus \partial\Omega_u$. For simplicity, our analysis focuses on displacement-controlled loading (i.e., Dirichlet boundary conditions), while noting that applied forces in load-controlled scenarios are equivalent to reaction forces under displacement control. The dataset comprises n_t snapshots of displacement measurements,

$$\left\{\boldsymbol{u}^{a,t} \in \mathbb{R}^3 \,:\, a = 1,\dots,n_n;\; t = 1,\dots,n_t\right\}, \tag{1}$$

recorded at n_n reference points comprising the measurement node set:

$$\left\{ \boldsymbol{X}^a \in \Omega : a = 1, \dots, n_n \right\}. \tag{2}$$

Additionally, for each snapshot, n_β reaction forces

$$\left\{ R^{\beta,t} \in \mathbb{R} : \beta = 1, \dots, n_\beta;\ t = 1, \dots, n_t \right\} \tag{3}$$

are measured at selected Dirichlet boundaries (e.g., using load cells). Since $n_\beta \ll n_n$, the reaction force data are sparse compared to the dense displacement field. For brevity, the superscript $(\cdot)^t$ is omitted in the subsequent discussion, although the numerical procedure is applied independently to every snapshot. Given $\{\boldsymbol{u}^a\}$ and $\left\{R^\beta\right\}$, our goal is to infer the parameter set $\boldsymbol{\theta}$ of an a priori assumed constitutive model $\psi(\boldsymbol{F}, \boldsymbol{\theta})$.

To connect the measurements to equilibrium, we first reconstruct a continuous kinematic field and its deformation gradient. The reference domain Ω is discretized using linear tetrahedral elements, evaluated with a single quadrature point at its barycenter, yielding

$$\boldsymbol{u}(\boldsymbol{X}) = \sum_{a=1}^{n_n} N^a(\boldsymbol{X})\, \boldsymbol{u}^a. \tag{4}$$

Here, $N^a : \Omega \to \mathbb{R}$ represents the shape function associated with the measurement node $\boldsymbol{X}^a$. We subsequently approximate the corresponding deformation gradient field as

$$\boldsymbol{F}(\boldsymbol{X}) = \boldsymbol{I} + \sum_{a=1}^{n_n} \boldsymbol{u}^a \otimes \nabla N^a(\boldsymbol{X}), \tag{5}$$

where $\boldsymbol{I}$ is the identity matrix, and ∇ represents the gradient operator with respect to the reference coordinates $\boldsymbol{X}$.

Assuming hyperelasticity, i.e., no dissipative energy losses within the material, the first Piola Kirchhoff stress follows as

$$\boldsymbol{P}(\boldsymbol{F}) = \frac{\partial \psi(\boldsymbol{F}, \boldsymbol{\theta})}{\partial \boldsymbol{F}} \tag{6}$$

as the constitutive relation between the first Piola Kirchhoff stress $\boldsymbol{P}$ and the deformation gradient $\boldsymbol{F}$ defined through the free energy function ψ and parameterized using the constitutive parameter set $\boldsymbol{\theta}$ [50–52]. In particular, $\boldsymbol{P}$ depends on the unknown parameters through $\psi(\boldsymbol{F}, \boldsymbol{\theta})$.

We leverage the conservation of linear momentum to guide the learning of the constitutive model parameter set, which eliminates the need for stress labels [30,31]. Assuming quasi-static loading conditions and negligible body forces, the weak form of the linear momentum balance in our reference domain Ω is given by

$$\int_\Omega \boldsymbol{P}(\boldsymbol{F}, \boldsymbol{\theta}) : \nabla \boldsymbol{v} \, \mathrm{d}V - \int_{\partial\Omega_t} \bar{\boldsymbol{t}} \cdot \boldsymbol{v} \, \mathrm{d}S = 0 \quad \forall \text{ admissible } \boldsymbol{v}, \tag{7}$$

where $\bar{\boldsymbol{t}}$ denotes the prescribed traction acting on $\partial\Omega_t$ per unit reference area and $\boldsymbol{v}$ is a test function that is sufficiently regular and vanishes on the Dirichlet boundary $\partial\Omega_u$. We prefer the weak formulation over the strong form, as it avoids the need for second order derivatives with respect to the displacement field, which are sensitive to measurement noise. In our displacement-controlled setting, non-instrumented free surfaces are typically traction free (so $\bar{\boldsymbol{t}} = 0$ there). Measured boundary forces enter through reactions on $\partial\Omega_u$, which we incorporate below.

Let $\mathcal{D} = \{(a, i) : a = 1, \dots, n_n;\ i = 1, 2, 3\}$ denote all the displacement degrees of freedom in our domain Ω, which we partition into $\mathcal{D}^{\text{free}}$, the unconstrained degrees of freedom, and $\mathcal{D}^{\text{fix}}_\beta$ (with $\beta = 1, \dots, n_\beta$) denoting the degrees of freedom under Dirichlet constraints that contribute to the observed reaction force R^β. Using a Bubnov–Galerkin discretization, we approximate the admissible test function $\boldsymbol{v}$ as

$$\boldsymbol{v}(\boldsymbol{X}) = \sum_{a=1}^{n_n} N^a(\boldsymbol{X})\, \boldsymbol{v}^a, \qquad \text{with} \quad v_i^a = 0 \quad \forall\ (a, i) \in \bigcup_{\beta=1}^{n_\beta} \mathcal{D}^{\text{fix}}_\beta, \tag{8}$$

and introducing our constitutive relation (6), our weak form (7) reduces to

$$\sum_{a=1}^{n_n} v_i^a f_i^a = 0, \quad \text{with} \quad f_i^a = \underbrace{\int_\Omega P_{ij} \nabla_j N^a \, \mathrm{d}V}_{\text{internal force}} - \underbrace{\int_{\partial\Omega_t} \bar{t}_i N^a \, \mathrm{d}S}_{\text{external force}}. \tag{9}$$

The integrals are evaluated by numerical quadrature on the same discretization as (4). Since the test functions are arbitrary on $\mathcal{D}^{\text{free}}$, the force residual must vanish at every unconstrained degree of freedom,

$$f_i^a = 0 \quad \forall\ (a, i) \in \mathcal{D}^{\text{free}}. \tag{10}$$

At the fixed degrees of freedom, the internal and external forces are counteracted by the reaction force imposed by the Dirichlet constraints. Because point-wise reactions are not accessible experimentally, we treat them as unavailable. Instead, we use the measured reaction forces integrated over instrumented boundary segments, which yields the global balance constraint

$$\sum_{(a,i) \in \mathcal{D}^{\text{fix}}_\beta} f_i^a = R^\beta \qquad \forall \qquad \beta = 1, \dots, n_\beta, \tag{11}$$

where the summation is carried out over all point-wise forces associated with the degrees of freedom in the βth Dirichlet constraint, denoted as $\mathcal{D}_\beta^{\text{fix}}$.

Together, (10) and (11) constitute a system of equations that defines the inverse problem of constitutive model inference [30,31,33]. We deterministically solve for $\boldsymbol{\theta}^\star$ by minimizing the equilibrium residuals over all snapshots:

$$\boldsymbol{\theta}^\star \leftarrow \arg\min_{\boldsymbol{\theta}} \sum_{t=1}^{n_t} \Bigg[\underbrace{\sum_{(a,i)\,\in\,\mathcal{D}^{\text{free}}} \left(f_i^{a,t}\right)^2}_{\text{free degrees of freedom}} + \underbrace{\sum_{\beta=1}^{n_\beta} \left(\lambda_r R^{\beta,t} - \sum_{(a,i)\,\in\,\mathcal{D}_\beta^{\text{fix}}} \lambda_r f_i^{a,t} \right)^2}_{\text{fixed degrees of freedom}} \Bigg], \tag{12}$$

such that the displacement and reaction force data satisfy the physics-based constraints (10) and (11).

2.2. Stochastic variational inference

In this study, we assume an a priori known constitutive law (33) and aim to infer $\pi\left(\boldsymbol{\theta}, \sigma^2, \upsilon_s \mid \boldsymbol{u}, \boldsymbol{R}\right)$, i.e. the posterior distribution of the constitutive parameter set $\boldsymbol{\theta}$ given the data $\{\boldsymbol{u}, \boldsymbol{R}\}$. Leveraging Bayes' theorem, we combine prior beliefs about $\boldsymbol{\theta}$ with a likelihood model that accounts for the impact of measurement noise on the physics-based residual constraints conditioned on the displacement and reaction force data.

We recast the deterministic optimization problem in (12) within a Bayesian inference framework by introducing the forward model $\boldsymbol{g}$, a convenient and vectorized form of f_i^a from (9), and define the measured set of reaction forces, $\boldsymbol{R}$, as

$$\boldsymbol{g}^t(\boldsymbol{\theta}) = \begin{bmatrix} \left\{ f_i^{a,t} \right\}_{(a,i)\in\mathcal{D}^{\text{free}}} \\ \left\{ \lambda_r \sum_{(a,i)\in\mathcal{D}_\beta^{\text{fix}}} f_i^{a,t} \right\}_{\beta=1}^{n_\beta} \end{bmatrix}, \quad \boldsymbol{R}^t = \begin{bmatrix} \{0\} \\ \left\{ \lambda_r R^{\beta,t} \right\}_{\beta=1}^{n_\beta} \end{bmatrix}, \tag{13}$$

for a given snapshot $t = 1, \ldots, n_t$. We stack all predicted snapshots and measured forces into two global vectors

$$\boldsymbol{g}(\boldsymbol{\theta}) = \begin{bmatrix} \boldsymbol{g}^1(\boldsymbol{\theta}) \\ \vdots \\ \boldsymbol{g}^{n_t}(\boldsymbol{\theta}) \end{bmatrix}, \quad \boldsymbol{R} = \begin{bmatrix} \boldsymbol{R}^1 \\ \vdots \\ \boldsymbol{R}^{n_t} \end{bmatrix} \tag{14}$$

This construction removes the need to carry superscript $(\cdot)^t$ in the subsequent probabilistic expressions while still retaining the multi-snapshot information. Note that $\boldsymbol{g}(\boldsymbol{\theta})$ implicitly depends on observed displacements through the constitutive response leading to the predicted forces in f_i^a.

We assume that the difference between the predicted and measured forces follow a multivariate normal distribution with zero mean and isotropic variance, reflecting the assumption of additive Gaussian noise:

$$\boldsymbol{R} = \boldsymbol{g}(\boldsymbol{\theta}) + \boldsymbol{\epsilon}, \quad \boldsymbol{\epsilon} \sim \mathcal{N}(\boldsymbol{0}, \sigma^2 \boldsymbol{I}) \tag{15}$$

which yields the likelihood

$$\pi\left(\boldsymbol{R} \mid \boldsymbol{\theta}, \sigma^2, \boldsymbol{u}\right) \propto \exp\left(-\frac{1}{2\sigma^2} \| \boldsymbol{g}(\boldsymbol{\theta}) - \boldsymbol{R} \|^2 \right) \tag{16}$$

In our case, both displacement field and reaction force measurements are affected by sensor noise, and we treat σ^2 as an effective residual variance that captures this combined uncertainty. Given that displacement propagates in a nonlinear fashion to the force residuals, we expect the residual variance to be dominated by displacement noise. We note here that the noise model adopted in the likelihood is an assumption, in accordance with related studies [32,53]. In practice, the true residual noise distribution could exhibit a more complex structure.

Next, we place priors on the residual noise variance σ^2 and the parameter vector $\boldsymbol{\theta}$. Typically, such variance is interpreted as a measurement error, but it can also consist of solver tolerance or discretization error especially when no measurement errors are assumed. Since the variance of the measurement noise σ^2 is unknown and must be inferred, we assign an inverse-gamma prior:

$$\sigma^2 \sim \mathcal{IG}\left(\alpha_\sigma, \beta_\sigma\right) \tag{17}$$

Concomitantly, we enforce physical constraints on the parameters by requiring them to be positive and therefore enforce a truncated normal distribution for the prior (truncated on the left at zero). Here, we introduce a scaling hyperprior υ_s to decouple the overall measurement residual noise variance σ^2 from the underlying parameter prior variance:

$$\boldsymbol{\theta} \sim \mathcal{N}_+\left(\boldsymbol{0}, \upsilon_s \sigma^2 \boldsymbol{I}\right) \tag{18}$$

We place an inverse-gamma hyperprior on υ_s:

$$\upsilon_s \sim \mathcal{IG}\left(\alpha_{\upsilon_s}, \beta_{\upsilon_s}\right) \tag{19}$$

The hierarchical structure [32,53,54] of our prior distributions is showcased in Fig. 2.

Combining the prior distributions (17)–(19) with the likelihood (16) yields the posterior:

$$\pi\left(\boldsymbol{\theta}, \sigma^2, \upsilon_s \mid \boldsymbol{u}, \boldsymbol{R}\right) = \frac{\pi\left(\boldsymbol{u}, \boldsymbol{R}, \boldsymbol{\theta}, \sigma^2, \upsilon_s\right)}{\pi\left(\boldsymbol{u}, \boldsymbol{R}\right)} = \frac{\pi\left(\boldsymbol{R} \mid \boldsymbol{\theta}, \sigma^2, \boldsymbol{u}\right)\, \pi\left(\boldsymbol{\theta} \mid \sigma^2, \upsilon_s\right)\, \pi\left(\sigma^2\right)\, \pi\left(\upsilon_s\right)}{\pi\left(\boldsymbol{u}, \boldsymbol{R}\right)}, \tag{20}$$

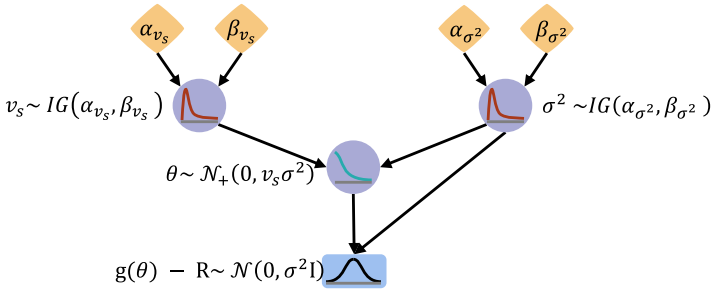

Fig. 2. Schematic of the hierarchical inference model. This hierarchical Bayesian model places priors on both the residual variance in the likelihood and the constitutive model parameters. The red circular distributions represent hyperpriors for v_s and σ^2, the light-blue circular distribution represents the prior on the material model parameters, and the black rectangular distribution represents the likelihood induced by the linear momentum balance residuals. The black arrows denote hierarchical dependencies. The hyperpriors are inverse-gamma distributed, the constitutive parameters are distributed according to a truncated multivariate normal distribution, and the likelihood is assumed to be normally distributed. (For interpretation of the references to color in this figure legend, the reader is referred to the web version of this article.)

This posterior can, in principle, be approximated using *sampling-based* inference or *variational inference*. In simpler inference problems, sampling-based methods such as MCMC can often be relied on to approximate the posterior distribution. For example, Gibbs sampling has been successfully applied to two-dimensional full-field problems, where the material response could be inferred by solving a linear system of equations on a library of constitutive features [32]. In those cases, the constitutive models were potentially nonlinear in input but remained linear in their parameters, which keeps the posterior geometry relatively tractable for MCMC. In our setting, however, the constitutive models are nonlinear in both inputs and parameters, which induces strong parameter interactions and complex (often multimodal) posteriors. Together with the cost of evaluating data-heavy 3D full-field likelihoods, this makes conventional MCMC-based posterior exploration computationally unattractive in practice.

We therefore adopt stochastic variational inference (SVI) to approximate the posterior efficiently using gradient-based optimization. SVI has been shown to substantially accelerate inference relative to MCMC in related settings [53,55].

More specifically, in SVI we approximate the posterior $\pi(\boldsymbol{\theta}, \sigma^2, v_s \mid \boldsymbol{u}, \boldsymbol{R})$ using a parametric guide family $q_{\boldsymbol{\Phi}}(\boldsymbol{\theta}, \sigma^2, v_s)$. To determine the best approximation within this variational family, we minimize the Kullback–Leibler (KL) divergence [56,57] between both distributions, i.e.,

$$\boldsymbol{\Phi}^\star \leftarrow \arg\min_{\boldsymbol{\Phi}} \mathrm{KL}\left(q_{\boldsymbol{\Phi}}(\boldsymbol{\theta}, \sigma^2, v_s) \parallel \pi(\boldsymbol{\theta}, \sigma^2, v_s \mid \boldsymbol{u}, \boldsymbol{R})\right). \tag{21}$$

Direct minimization of (21) is intractable because the posterior density depends on the marginal likelihood $\pi(\boldsymbol{u}, \boldsymbol{R})$, as shown in (20). Applying the definition of the KL divergence gives

$$\mathrm{KL}\left(q_{\boldsymbol{\Phi}}(\boldsymbol{\theta}, \sigma^2, v_s) \parallel \pi(\boldsymbol{\theta}, \sigma^2, v_s \mid \boldsymbol{u}, \boldsymbol{R})\right) = \mathbb{E}_{q_{\boldsymbol{\Phi}}}\left[\log \frac{q_{\boldsymbol{\Phi}}(\boldsymbol{\theta}, \sigma^2, v_s)}{\pi(\boldsymbol{\theta}, \sigma^2, v_s \mid \boldsymbol{u}, \boldsymbol{R})}\right]. \tag{22}$$

Substituting the posterior from (20) and separating numerator and denominator inside the logarithm yields

$$\mathrm{KL}\left(q_{\boldsymbol{\Phi}}(\boldsymbol{\theta}, \sigma^2, v_s) \parallel \pi(\boldsymbol{\theta}, \sigma^2, v_s \mid \boldsymbol{u}, \boldsymbol{R})\right) = -\mathcal{L}(\boldsymbol{\Phi}) + \log \pi(\boldsymbol{u}, \boldsymbol{R}), \tag{23}$$

where

$$\mathcal{L}(\boldsymbol{\Phi}) := \mathbb{E}_{q_{\boldsymbol{\Phi}}}\left[\log \pi(\boldsymbol{u}, \boldsymbol{R}, \boldsymbol{\theta}, v_s, \sigma^2) - \log q_{\boldsymbol{\Phi}}(\boldsymbol{\theta}, \sigma^2, v_s)\right]. \tag{24}$$

is the evidence lower bound (ELBO). This reformulation is useful because the marginal likelihood $\pi(\boldsymbol{u}, \boldsymbol{R})$, i.e. the evidence, no longer appears inside the optimization objective: it is constant with respect to $\boldsymbol{\Phi}$. As a result, minimizing the KL divergence in (21) is equivalent to maximizing the ELBO,

$$\boldsymbol{\Phi}^\star \leftarrow \arg\max_{\boldsymbol{\Phi}} \mathcal{L}(\boldsymbol{\Phi}). \tag{25}$$

Equivalently, and using that the KL divergence is non-negative,

$$\log \pi(\boldsymbol{u}, \boldsymbol{R}) = \mathcal{L}(\boldsymbol{\Phi}) + \mathrm{KL}\left(q_{\boldsymbol{\Phi}}(\boldsymbol{\theta}, \sigma^2, v_s) \parallel \pi(\boldsymbol{\theta}, \sigma^2, v_s \mid \boldsymbol{u}, \boldsymbol{R})\right), \tag{26}$$

which shows that $\mathcal{L}(\boldsymbol{\Phi})$ is indeed a lower bound on the log-evidence. In practice, this converts an intractable posterior-divergence minimization into a tractable variational optimization problem, since $\mathcal{L}(\boldsymbol{\Phi})$ depends only on the joint density $\pi\left(\boldsymbol{u}, \boldsymbol{R}, \boldsymbol{\theta}, v_s, \sigma^2\right)$ and the chosen guide distribution $q_{\boldsymbol{\Phi}}\left(\boldsymbol{\theta}, \sigma^2, v_s\right)$.

What remains is to choose a suitable guide distribution to approximate the posterior. We employ a mean-field variational family $q_{\boldsymbol{\Phi}}$ [58,59], which assumes statistical independence between the quantities of interest,

$$q_{\boldsymbol{\Phi}}\left(\boldsymbol{\theta}, \sigma^2, v_s\right) = q\left(\boldsymbol{\theta}\right) q\left(\sigma^2\right) q\left(v_s\right) \tag{27}$$

Table 1
Hyperparameters and simulation settings used in the stochastic variational inference framework and synthetic tissue slab data generation. The upper rows list optimization settings and hierarchical Bayesian prior parameters used for the SVI guide distributions and model priors. The bottom rows summarize the geometry and loading conditions for the training and validation slab specimens, respectively.

Parameter	Notation	Value
SVI hyperparameters:		
Weight for reaction force balance	λ_r	10
Optimizer	–	Adam
Number of epochs	n_T	20,000
Learning rate scheduler	–	Exponential
Base learning rate	r_0	0.01
Learning decay rate	γ	0.1
SVI guide hyperparameters:		
Initial mean of $\mathcal{N}_+$ distribution	μ_θ	$10^{-2} + \epsilon^2 \times \{1, \dots, 1\}, \quad \epsilon \sim \mathcal{N}(0, 0.1)$
Initial variance of $\mathcal{N}_+$ distribution	σ_θ^2	$10^{-18} \times \{1, \dots, 1\}$
Initial scale parameter for υ_s	α_{υ_s}	10^4
Initial rate parameter for υ_s	β_{υ_s}	10^4
Initial scale parameter for σ^2	a_{σ^2}	10^4
Initial rate parameter for σ^2	b_{σ^2}	10^4
SVI model prior hyperparameters:		
Prior mean of $\mathcal{N}_+$ distribution	μ_θ	$10^{-10} \times \{1, \dots, 1\}$
prior variance of $\mathcal{N}_+$ distribution	σ_θ^2	$\{1, \dots, 1\}$
prior scale parameter for υ_s	α_{υ_s}	1
prior rate parameter for υ_s	β_{υ_s}	1
prior scale parameter for σ^2	α_{σ^2}	1
prior rate parameter for σ^2	β_{σ^2}	1
Training slab specimen:		
Number of nodes in mesh for FEM-based data generation	–	16,856
Number of reaction force constraints	n_β	5
Number of data snapshots	n_t	2
Loading parameter	δ	$\{0.5 \times t : t = 2, 3\}$
Loading ratios	–	$\{(1:2), (1:1), (2:1)\}$
Ground-truth material model parameters θ_{gt}:		
Linear scaling parameters $a_\star$ [MPa]	a, a_f, a_n, a_{fs}	$\{0.809, 1.911, 0.227, 0.547\} \times 10^{-3}$
Exponential scaling parameters $b_\star$ [–]	b, b_f, b_n, b_{fs}	$\{7.474, 22.063, 34.802, 5.691\}$
Bulk modulus [MPa]	K	0.1

with factors:

$$q(\boldsymbol{\theta}) = \mathcal{N}_+(\boldsymbol{\mu}^q, \boldsymbol{\Sigma}^q \circ \boldsymbol{I}) \tag{28}$$

$$q(\sigma^2) = \mathcal{IG}\left(\alpha^q_{\sigma^2}, \beta^q_{\sigma^2}\right) \tag{29}$$

$$q(\upsilon_s) = \mathcal{IG}\left(\alpha^q_{\upsilon_s}, \beta^q_{\upsilon_s}\right), \tag{30}$$

where $\circ$ denotes the element-wise Hadamard product. The full set of variational parameters is denoted by $\boldsymbol{\Phi} = \left\{\boldsymbol{\mu}^q, \boldsymbol{\Sigma}^q, \alpha^q_{\sigma^2}, \beta^q_{\sigma^2}, \alpha^q_{\upsilon_s}, \beta^q_{\upsilon_s}\right\}$, and hyperparameters are reported in Table 1. We specifically highlight $\boldsymbol{\mu}^q$, and $\boldsymbol{\Sigma}^q$ to be the location and scale parameters of the truncated normal distribution. These correspond to the mean and standard deviation of the underlying and untruncated normal distribution used in the definition of $\mathcal{N}_+$.

The entire inference pipeline is implemented in `NumPyro` [60], enabling automatic differentiation and stochastic optimization with ADAM [61,62]. Doing so, we alleviate the need to explicitly define the minimization procedure as was done in Thorat et al. [53]. We initialize the optimizer with a learning rate of $r_0 = 0.01$, and apply an exponential learning rate decay γ, i.e. $r_i = r_0 \gamma^{i/n_T}$ at epoch i with n_T denoting the total number of epochs. The parameter λ_r was heuristically set to 10 after preliminary checks indicated stable parameter fitting behavior. A sensitivity study indicated that increasing the number of snapshots n_t beyond two did not improve validation performance (see Appendix H).

3. Synthetic data generation

To assess our Bayesian inference framework under controlled conditions, we generate synthetic biaxial tensile testing data from high-resolution simulations of varying microstructurally and geometrically heterogeneous myocardial tissue slabs.

3.1. Myofiber architecture and tissue slab slicing

Informed by prior histological characterizations of myocardial tissue [8,9,14], we model our studied specimens as a layered orthotropic material in which cardiomyocytes align along main myofiber directions, packed by endomysial collagen into sheets,

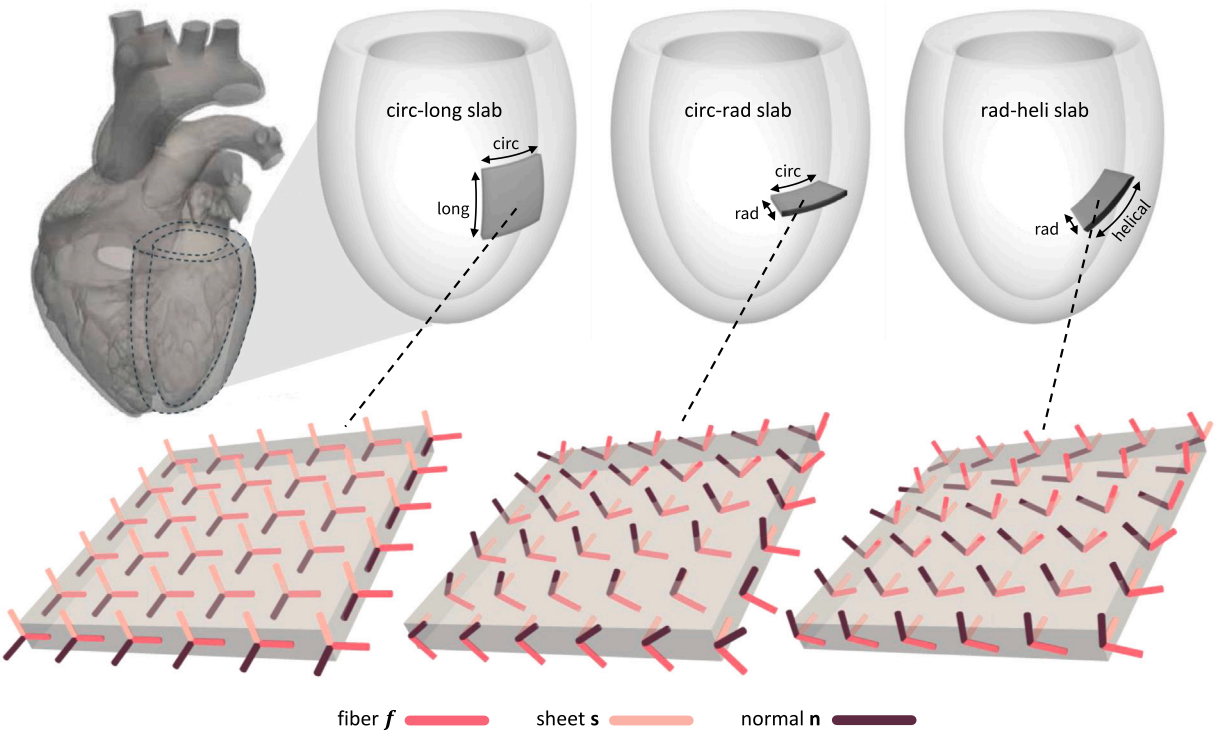

Fig. 3. Specimen slicing and microstructural organization. Top: Schematic of the left ventricle and three considered slicing orientations to extract myocardial tissue slabs: circumferential–longitudinal (*circ-long*), circumferential–radial (*circ-rad*), and a rotated variant of the latter (*rad-heli*). Bottom: Each slicing orientation leads to a distinct microstructural configuration within the specimen. In *circ-long* slabs, the fiber direction lies in-plane and the sheet direction spans the through-thickness. *Circ-rad* slabs display a transmural fiber rotation from epicardium to endocardium, with the sheet direction aligned in the radial plane. The *rad-heli* orientation rotates the slab around the radial axis, aligning all three microstructural directions approximately within the plane of the specimen. Fiber directions ($\boldsymbol{f}$) are shown in red, sheet directions ($\boldsymbol{s}$) in pink, and normal directions ($\boldsymbol{n}$) in brown. (For interpretation of the references to color in this figure legend, the reader is referred to the web version of this article.)

and connected via perimysial collagen. This organization defines three locally orthogonal directions: the fiber direction $\boldsymbol{f}$, the sheet direction $\boldsymbol{s}$, and the sheet-normal direction $\boldsymbol{n}$. To investigate the role of heterogeneity in unsupervised constitutive parameter identifiability, we simulate myocardial tissue slabs that exhibit both *microstructure*-induced and *geometry*-induced heterogeneity.

Leveraging the intrinsic spatially varying myofiber architecture in the human heart [63], we extract three microstructurally distinct synthetic tissue slabs from the left ventricular free wall. All samples are assumed to be $10\times10\times1$ mm^3 in size, representative of slabs from a healthy human left ventricular wall. These slab dimensions should be interpreted as an idealized benchmark geometry for controlled 3D full-field constitutive inference. We further detail the sample geometry and applied boundary conditions in Appendix A.

Fig. 3 showcases the microstructural variability across the slab domain, with directional fiber $\boldsymbol{f}$, sheet $\boldsymbol{s}$ and normal $\boldsymbol{n}$ vectors discretized element-wise, and their spatial distribution depends on the chosen slicing orientation:

- **circ-long:** sections aligned with the ventricular circumferential–longitudinal plane. The in-plane $\boldsymbol{f}$ orientation and through-thickness $\boldsymbol{s}$ direction enable near-planar fiber alignment. We consider both aligned and off-axis variants depending on their angular deviation from the square edge. This slab specimen type aligns with the biaxial tension testing slabs studied by [11].
- **circ-rad:** sections cut in the circumferential–radial plane. These samples exhibit a transmural fiber rotation from approximately $-60°$ at the epicardium to $+60°$ at the endocardium, while the sheet direction $\boldsymbol{s}$ remains in-plane and radially aligned.
- **rad-heli:** samples based on a radial-helical cut. Given the natural transmural variation of the myofiber angle $\boldsymbol{f}$ from $-60°$ in the sub-epicardium to $+60°$ in the sub-endocardium [63], this configuration places all three microstructural directions ($\boldsymbol{f}, \boldsymbol{s}, \boldsymbol{n}$) approximately within the sample plane by rotating the sample an additional 45° along the radial axis. The resultant fiber orientation ranges from $-15°$ up to 105°, aligning the $\boldsymbol{f}$ fiber in the sample plane near the bottom edge of the sample and aligning the $\boldsymbol{n}$ fiber in the sample plane near the top edge.

To investigate the influence of geometric heterogeneity, we introduce a second set of specimens with a central circular occlusion with a radius of 1 mm, see Appendix A. These samples are expected to introduce additional deformation heterogeneity that we

hypothesize may improve constitutive parameter identifiability under limited data conditions, e.g., when inferring orthotropic behavior from a single biaxial tensile test.

3.2. Biaxial loading emulation

We simulate a digital volume correlation experiment by modeling a biaxial loading protocol on the microstructurally and geometrically homogeneous and heterogeneous tissue slabs described above using the finite element method (FEM) implemented in ABAQUS/Standard [64], see for example [26]. Our virtual tissue slabs are subjected to displacement-controlled symmetric biaxial loading, with loading ratios $\lambda_1 : \lambda_2 = (1:2), (1:1), (2:1)$ defined in terms of the prescribed edge stretches along the two in-plane loading directions. The maximum stretch applied to the samples is 15% of the initial edge length, consistent with maximal values used in experiments [11]. We use linear tetrahedral elements to discretize the domain and record nodal displacements along with reaction forces for a sequence of n_t load steps (see Figure A.1)

To define the constitutive response, we use the local volume change $J = \det(\boldsymbol{F})$ and multiplicatively decompose the deformation gradient $\boldsymbol{F}$ (5) into its volumetric $\boldsymbol{F}^{\text{vol}}$ and isochoric $\bar{\boldsymbol{F}}$ parts [65],

$$\boldsymbol{F} = \boldsymbol{F}^{\text{vol}}\bar{\boldsymbol{F}} \quad \text{with} \quad \boldsymbol{F}^{\text{vol}} = J^{\frac{1}{3}}\boldsymbol{I} \quad \text{and} \quad \bar{\boldsymbol{F}} = J^{-\frac{1}{3}}\boldsymbol{F}. \tag{31}$$

We then introduce the following deformation (pseudo-)invariants [66,67]:

$$\begin{aligned} \bar{I}_1 &= [\bar{\boldsymbol{F}}^{\mathrm{T}}\bar{\boldsymbol{F}}] : \boldsymbol{I} \\ \bar{I}_{4\mathrm{ff}} &= [\bar{\boldsymbol{F}}^{\mathrm{T}}\bar{\boldsymbol{F}}] : [\boldsymbol{f}^0 \otimes \boldsymbol{f}^0] \\ \bar{I}_{4\mathrm{nn}} &= [\bar{\boldsymbol{F}}^{\mathrm{T}}\bar{\boldsymbol{F}}] : [\boldsymbol{n}^0 \otimes \boldsymbol{n}^0] \\ \bar{I}_{4\mathrm{fs}} &= [\bar{\boldsymbol{F}}^{\mathrm{T}}\bar{\boldsymbol{F}}] : [\boldsymbol{f}^0 \otimes \boldsymbol{s}^0] \end{aligned} \tag{32}$$

where $\boldsymbol{f}^0$, $\boldsymbol{s}^0$, $\boldsymbol{n}^0$ denote the local microstructure fiber, sheet, and normal unit vector orientations in the undeformed reference configuration. We adopt the orthotropic, compressible Holzapfel-Ogden (HO) material model [14,15] using the following strain energy density function:

$$\begin{aligned} \psi(\boldsymbol{F}, \boldsymbol{\theta}) = &\frac{a}{2b}\left[\exp\left(b(\bar{I}_1 - 3)\right) - 1\right] + \sum_{i=f,n}\frac{a_i}{2b_i}\left[\exp\left(b_i\left\langle \bar{I}_{4ii} - 1\right\rangle^2\right) - 1\right] \\ &+ \frac{a_{fs}}{2b_{fs}}\left[\exp\left(b_{fs}\bar{I}_{4fs}^2\right) - 1\right] + \frac{K}{2}\left(\frac{J^2 - 1}{2} - \ln J\right) \end{aligned} \tag{33}$$

to compute the First Piola Kirchhoff stress tensor $\boldsymbol{P}$ following (6). Note that this variation from Guan et al. relies on the invariant I_{4nn}, whereas the original model used the invariant I_{4ss}. This variation of the HO-model was implemented using the recently proposed universal user material subroutine in Abaqus [52].

In (33), $\boldsymbol{\theta} = \{a, b, a_f, b_f, a_n, b_n, a_{fs}, b_{fs}, K\}$ (see Table 1) denotes the to-be-inferred ground-truth material parameters. The Macaulay brackets $\langle x \rangle$ ensure that fiber and sheet term strain energy contributions activate only under tension [52,68,69]. Lastly, a bulk modulus is chosen based on the distribution of J in the *circ-long-hom* samples and common compressibility considerations of the myocardium [70,71] to limit volumetric strains while retaining numerical stability.

To quantify how microstructural and geometric heterogeneity enrich the deformation space relevant for inference, Figs. 4–5 report the resulting distributions of the key invariants activated under biaxial loading, which motivates our single-test identification setup.

Fig. 4 presents the deformation response of geometrically homogeneous slabs with varying microstructural architectures. The qualitative results of the maximum principal stretch are shown for all loading conditions and homogeneous tissue samples. On the right side of the figure we show kernel density estimations of the biaxially activated invariants, truncated at 20 to visualize the spread of these invariants. The *circ-long-hom* configuration represents a classic homogenized myocardial sample, as excised by [11], with assumed uniform fiber-sheet-normal orientations. Under biaxial loading, this results in a uniform deformation pattern with isotropic invariants I_1 ranging from 3.158 to 3.257 across the three loading protocols. Anisotropic contributions are moderate, with I_{4ff} and I_{4nn} spanning ranges from 1.025 to 1.139 and 1.024 to 1.144 respectively. Fiber-sheet shear contributions remain negligible, with I_{4fs} limited to 0.000 up to machine precision. Introducing transmural fiber variation in the *circ-rad-hom* slab increases local deformation heterogeneity. The isotropic deformation invariant I_1 expands to a broader range of 3.160 to 3.367, while I_{4ff} and I_{4nn} reach 1.194 and 1.252, respectively. Notably, fiber-sheet shear contributions increase, with I_{4fs} reaching up to 0.099. In the *rad-heli-hom* specimen, which introduces a more asymmetric helical fiber distribution, deformation heterogeneity is further amplified. The isotropic invariant I_1 ranges from 3.147 to 3.359, while I_{4ff} increases significantly, spanning up to 1.248. The I_{4nn} component reaches 1.251, and fiber-sheet shear contributions grow to 0.114. The distributions of invariants shown in the right column of Fig. 4 emphasize these trends. The *circ-long-hom* specimen exhibits single homogeneous singular values for I_{4ff} and I_{4nn}, while I_{4fs} remains zero. In contrast, *circ-rad-hom* and *rad-heli-hom* configurations display broader distributions across all invariants, particularly for fiber-sheet shear deformations. Consistent with these observations, we note tissue bulging effects in the thickness direction. *Circ-rad* configurations exhibit bulging centrally, whereas rad-heli configurations deform near the specimen edges. In particular, the *rad-heli-hom* configuration shows noticeable thickness bulging coinciding with bands of reduced strain, where fibers align in-plane. Overall, microstructure-induced heterogeneity alone enriches the activated invariant space under a single biaxial protocol, which motivates using these slabs as training configurations in this study.

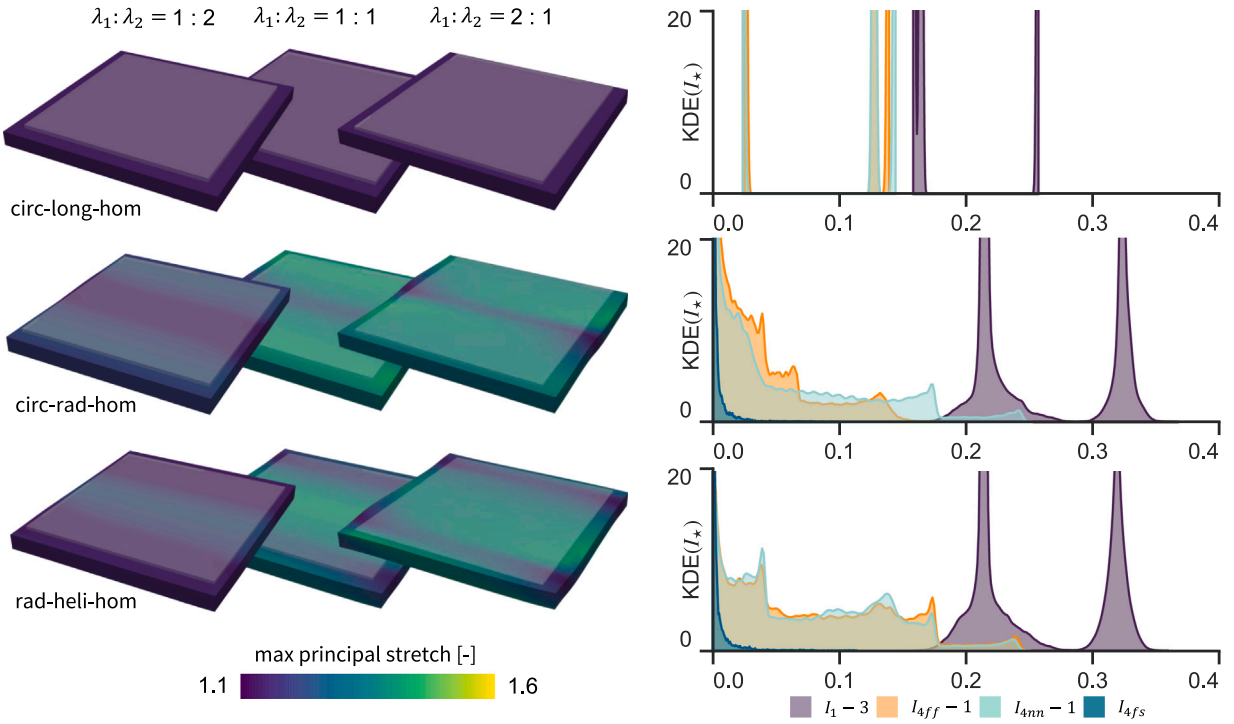

Fig. 4. Deformation profiles of geometrically homogeneous tissue slabs with varying microstructural heterogeneity. Maximum principal stretches are shown for *circ-long-hom* (top row), *circ-rad-hom* (middle row), and *rad-heli-hom* (bottom row) specimens subjected to biaxial loading protocols ($\lambda_1 : \lambda_2 = (1:2), (1:1), (2:1)$) up to $\lambda^{\max} = 1.15$. Rightmost columns display distributions of invariants $I_1 - 3$, $I_{4ff} - 1$, $I_{4nn} - 1$, and I_{4fs} for each specimen type respectively using approximated kernel density estimations denoted as KDE(I_*). The kernel density estimation is truncated at an arbitrary level of 20 to show the spread of the invariants more clearly.

Fig. 5 illustrates the deformation response of geometrically heterogeneous slabs, where a central occlusion is combined with varying microstructural organization. In the *circ-long-het* specimen, geometric heterogeneity alone induces significant deformation diversity. The isotropic invariant I_1 spans from 3.070 to 3.390, with I_{4ff} and I_{4nn} reaching up to 1.232 and 1.209, respectively. Fiber-sheet shear contributions, represented by I_{4fs}, remain limited, peaking at 0.034. Adding microstructural heterogeneity in the *circ-rad-het* configuration further amplifies deformation heterogeneity. Here, I_1 varies between 3.141 and 3.5477, while I_{4ff} and I_{4nn} attain maximum principal stretches of 1.218 and 1.243 respectively. Notably, fiber-sheet shear contributions increase substantially, with I_{4fs} rising to 0.4342. In the *rad-heli-het* specimen, characterized by asymmetric helical fiber variation and geometric heterogeneity, isotropic I_1 deformation spans 3.136 to 3.518. Anisotropic contributions reach 1.242 for I_{4ff}, 1.241 for I_{4nn}, and 1.289 for the fiber-sheet shear term I_{4fs}, which confirms this configuration as the most mechanically diverse. The distributions of invariants reflect these differences. The *circ-long-het* slab shows moderate spreading compared to its homogeneous counterpart, but fiber-sheet shearing remains limited. In contrast, the *circ-rad-het* and *rad-heli-het* configurations exhibit pronounced broadening in all invariants, particularly in I_{4fs}, underscoring the synergistic effect of combined geometrical and microstructural heterogeneities. Similar to the homogeneous cases, bulging effects are evident. *Circ-rad* configurations exhibit central bulging, while *rad-heli* configurations deform near specimen edges. The *rad-heli-het* specimen shows the most pronounced bulging, exceeding initial thickness. Localized deformation bands with reduced strain are again visible, while regions surrounding the central occlusion display elevated strains, highlighting the amplification of local deformation due to geometric discontinuities. These observations reinforce the rationale for using such heterogeneous configurations as training specimens, enhancing parameter identifiability through enriched mechanical diversity.

4. Inference results and robustness to measurement noise

In this section, we assess the training and fitting performance of the method. We track the evolution of the fit over optimization epochs and compute error metrics from the inferred posterior. The convergence of the posterior standard deviations of the material parameters was verified, confirming that the uncertainty estimates stabilize prior to the final optimization epoch and for the results reported here. We then assess robustness under both spatially uncorrelated and spatially correlated displacement perturbations.

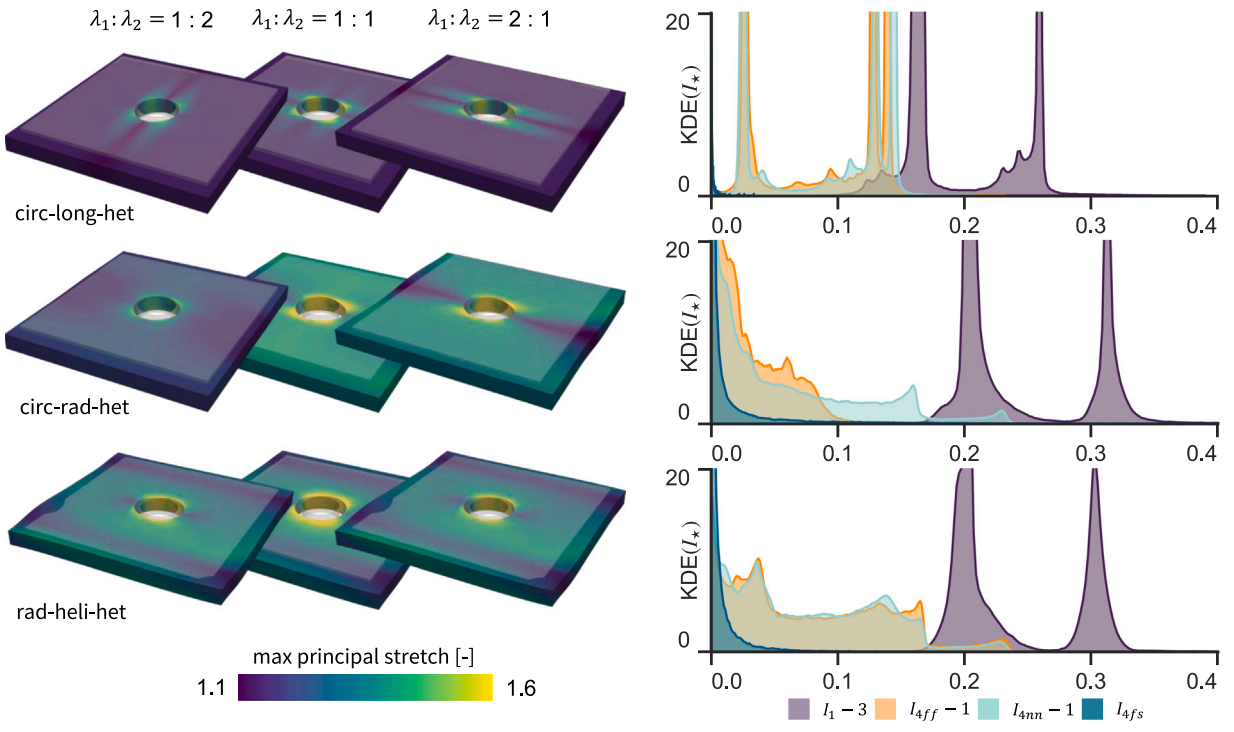

Fig. 5. Deformation profiles of geometrically and microstructurally heterogeneous tissue slabs. Maximum principal stretches *circ-long-het* (top row), *circ-rad-het* (middle row), and *rad-heli-het* (bottom row) specimens under biaxial loading ($\lambda_1 : \lambda_2 = (1:2), (1:1), (2:1)$). Invariant distributions of $I_1 - 3$, $\bar{I}_{4ff} - 1$, $\bar{I}_{4nn} - 1$, and I_{4fs} are shown in the rightmost panels using approximated kernel density estimations denoted as KDE(I_*). The kernel density estimation is truncated at an arbitrary level of 20 to show the spread of the invariants more clearly.

4.1. Noise-free inference: identifiability gains from microstructural and geometrical heterogeneity

Figs. 6 and 7 summarize the inference performance of our framework in recovering the ground-truth HO parameter set $\boldsymbol{\theta}_{\text{gt}}$ (Table 1) based on combined full-field deformation and reaction force data. Each figure shows, from top to bottom: (i) the evolution of the inferred parameters' guide location μ_θ over optimization epochs, (ii) the corresponding absolute relative errors e_{μ_θ}, (iii) final relative errors after convergence, and (iv) posterior distributions $\tilde{\theta}$, scaled to highlight skewness and relative spread. Here, we highlight posterior distributions in color when the unbiased skewness value $|s_{\tilde{\theta}}|$ is strictly greater than 0.5. We define the following four metrics: the relative point error metric $\hat{e}_\theta$ between the mean of the underlying and untruncated normal distribution and the ground truth, and the relative error e_θ between samples from the posterior and the ground truth:

$$\hat{e}_\theta = \frac{\mu_\theta - \theta_{\text{gt}}}{\theta_{\text{gt}}} \qquad e_\theta = \frac{\theta - \theta_{\text{gt}}}{\theta_{\text{gt}}} \tag{34}$$

Here, we define $\mu_\theta = \mu^q$ as the mean of the underlying untruncated normal distribution used in the guide distribution. Furthermore, we define the unbiased skewness s_θ:

$$s_{\tilde{\theta}} = \frac{\sqrt{N(N-1)}}{N-2} \cdot \frac{\frac{1}{N}\sum_{n=1}^{N}(\tilde{\theta}_n - \mu_{\tilde{\theta}})^3}{\left(\frac{1}{N}\sum_{n=1}^{N}(\tilde{\theta}_n - \mu_{\tilde{\theta}})^2\right)^{3/2}} \qquad \text{with} \qquad \tilde{\theta} = \frac{\theta - \mu_\theta}{\mu_\theta} \tag{35}$$

with $\tilde{\theta}$ denoting the relative error between samples taken from the guide distribution and the scaled posterior, $\mu_{\tilde{\theta}}$ denoting the mean of the distribution $\tilde{\theta}$, and N equaling the number of samples drawn from the posterior distribution. Unless stated otherwise, we draw $N = 1000$ samples from the inferred guide distribution shown in the bottom rows of Figs. 6 and 7, respectively, to visualize the shape, mean, and spread of the approximated posterior distribution. For completeness, the full set of converged parameter estimates, posterior scales (the standard deviation of the underlying and untruncated normal distribution), and relative errors for all six training specimens is reported in Appendix E (Tables E.3–E.4). In the main text, we therefore focus on the parameter groups that drive the qualitative differences between Figs. 6 and 7, and summarize the remaining terms compactly.

Focusing on the *geometrically homogeneous* specimens (Fig. 6), the plots show rapid convergence and narrow posteriors for the isotropic (a, b, K) and primary anisotropic (a_f, b_f, a_n, b_n) parameter groups across all three microstructural settings. Quantitatively,

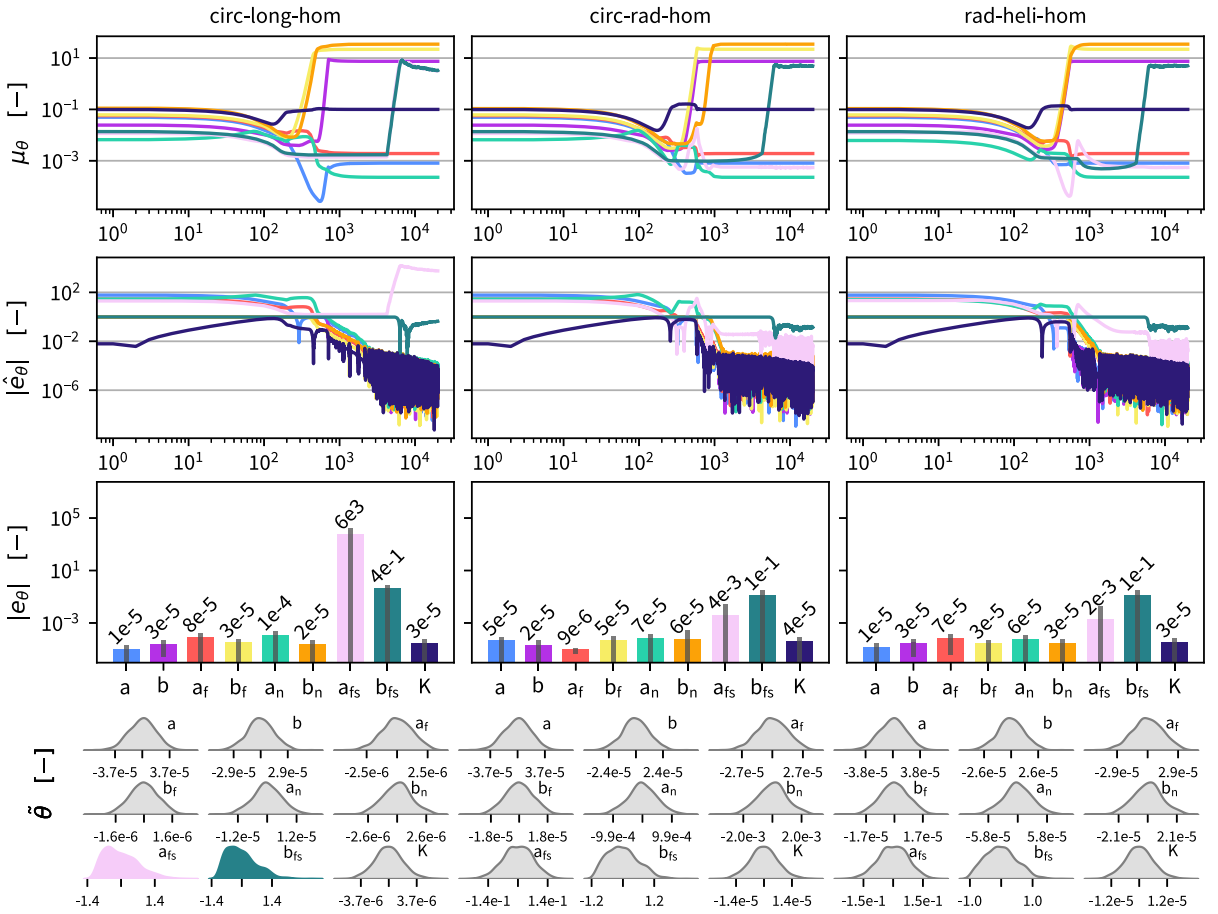

Fig. 6. Noise-free parameter inference on geometrically homogeneous and microstructurally heterogeneous tissue slabs. From left to right: *circ-long-hom*, *circ-rad-hom*, and *rad-heli-hom* specimens. From top to bottom: (i) evolution of inferred material parameters θ over optimization epochs, (ii) evolution of absolute relative location parameter errors $|\hat{e}_\theta|$, (iii) absolute relative errors $|e_\theta|$ at the final epoch with corresponding 95% credibility interval, and (iv) rescaled posterior distributions $\tilde{\theta}$ (drawn from the variational guide). The plots show rapid convergence and small final errors for most parameters across all three specimens, while the shear-coupling parameters (a_{fs}, b_{fs}) display slower convergence and broader posteriors in several cases. Distributions are shown in grayscale when the absolute unbiased skewness satisfies $|s_{\tilde{\theta}}| < 0.5$. (For interpretation of the references to color in this figure legend, the reader is referred to the web version of this article.)

these parameters reach small final deviations, with the largest magnitudes remaining below 3.477×10^{-2} in this homogeneous-geometry group (Table E.4). In contrast, the fiber–sheet shear-coupling terms (a_{fs}, b_{fs}) are the dominant outliers. In the fully homogeneous *circ-long-hom* specimen, the shear-coupling terms remain poorly identified, with large final errors ($\hat{e}_{a_{fs}} = -5.738 \times 10^{3}$ and $\hat{e}_{b_{fs}} = 4.279 \times 10^{-1}$; Table E.4).

Introducing transmural and helical fiber variation improves identifiability of a_{fs} substantially (from $\mathcal{O}(10^3)$ to $\mathcal{O}(10^{-3} - 10^{-2})$; Table E.4), while b_{fs} remains the least accurate inferred parameter in the homogeneous-geometry group (e.g., $\hat{e}_{b_{fs}} = 1.354 \times 10^{-1}$ for *circ-rad-hom* and 1.283×10^{-1} for *rad-heli-hom*). Notably, b_{fs} also converges more slowly than the remaining parameters: it stabilizes only after ∼14 000 epochs in *circ-rad-hom*, whereas most other parameters stabilize within ∼1000 epochs (rows (i)–(ii)). These trends are consistent with the broader and more skewed posteriors for (a_{fs}, b_{fs}) in Fig. 6 (bottom row).

For the *geometrically heterogeneous* specimens (Fig. 7), the plots show stable convergence across parameter groups and generally narrower posterior spreads than in Fig. 6. For the isotropic and primary anisotropic parameters, final deviations remain small overall, with the largest magnitudes staying below 9.178×10^{-5} across the heterogeneous-geometry group (Table E.4). The most pronounced quantitative change occurs in the inferred shear-coupling parameters. With combined geometric heterogeneity and fiber rotation, both a_{fs} and b_{fs} converge to small final deviations: in *circ-rad-het*, $\hat{e}_{a_{fs}} = -1.459 \times 10^{-3}$ and $\hat{e}_{b_{fs}} = -7.901 \times 10^{-4}$, and in *rad-heli-het*, $\hat{e}_{a_{fs}} = -1.505 \times 10^{-3}$ and $\hat{e}_{b_{fs}} = 2.882 \times 10^{-3}$ (Table E.4). In contrast, without fiber rotation (*circ-long-het*), b_{fs} remains comparatively inaccurate ($\hat{e}_{b_{fs}} = 4.471 \times 10^{-1}$), consistent with the broader posterior in the corresponding column of Fig. 7. Compared with the homogeneous-geometry cases in Fig. 6, the rotated-fiber heterogeneous specimens (*circ-rad-het* and *rad-heli-het*) reach a stable b_{fs} trajectory with small final deviations within 1000 epochs, rather than requiring ∼14 000 epochs, consistent with the tighter posterior spreads in row (iv).

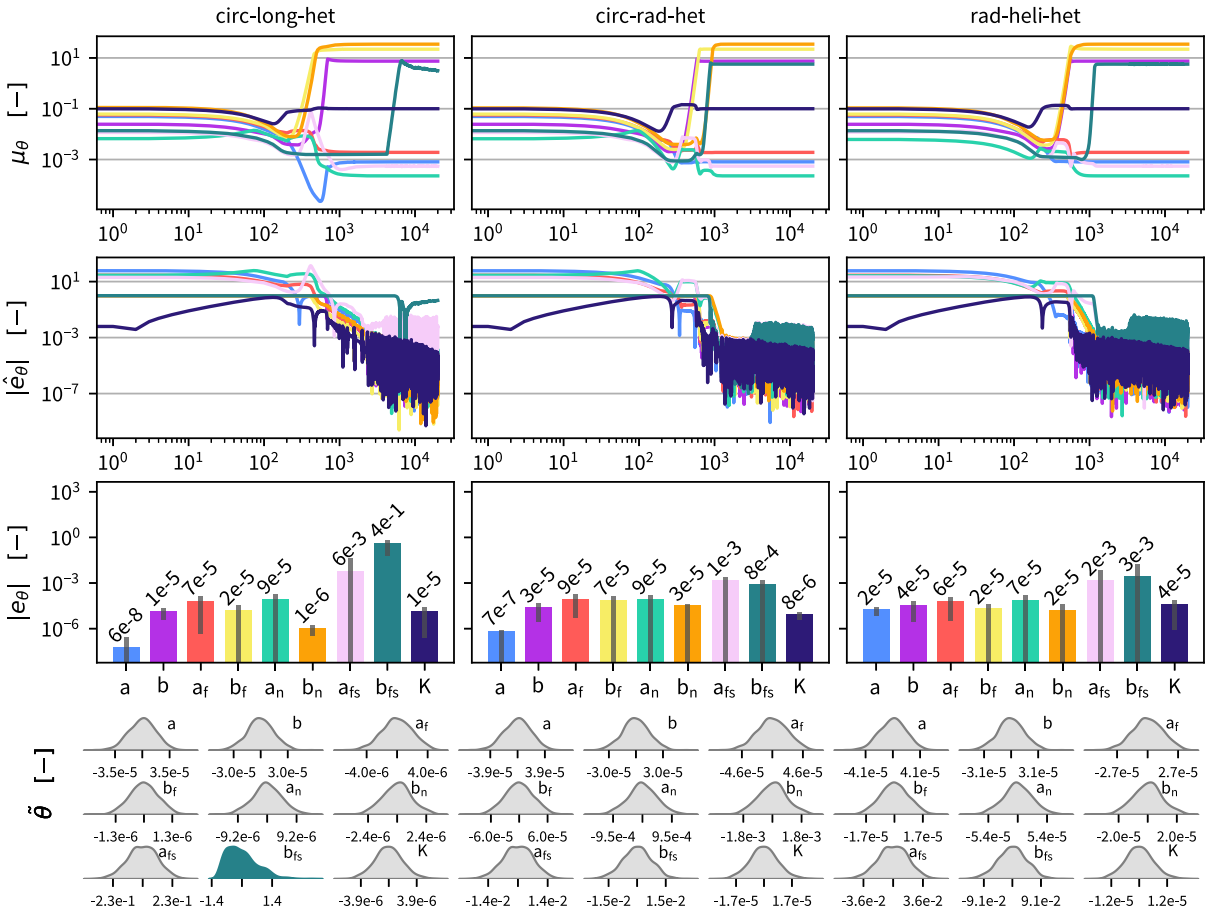

Fig. 7. Noise-free parameter inference on geometrically and microstructurally heterogeneous tissue slabs. From left to right: *circ-long-het*, *circ-rad-het*, and *rad-heli-het* specimens. From top to bottom: (i) evolution of inferred material parameters θ over optimization epochs, (ii) evolution of absolute relative location parameter errors $|\hat{e}_\theta|$, (iii) absolute relative errors $|e_\theta|$ at the final epoch with corresponding 95% credibility interval, and (iv) rescaled posterior distributions $\tilde{\theta}$ (drawn from the variational guide). The plots show stable convergence for all parameter groups across the three specimens, and the posterior samples indicate narrower spreads for the shear-coupling parameters (a_{fs}, b_{fs}) compared with the homogeneous counterparts. Distributions are shown in grayscale when the absolute unbiased skewness satisfies $|s_{\tilde{\theta}}| < 0.5$. (For interpretation of the references to color in this figure legend, the reader is referred to the web version of this article.)

Across both Figs. 6 and 7, several parameters exhibit non-monotonic transients before converging. In particular, multiple traces (including b, b_f, a_n, and a_{fs}) show a decrease after roughly 10^2 epochs, followed by recovery towards their converged values by $\mathcal{O}(10^3)$ epochs. Consistent excursions appear in the error plots over the same epoch range, reflecting epochs where the inferred trajectories pass through the ground-truth value (i.e., where the signed relative deviation changes sign) without immediately stabilizing. This behavior is consistent with strong parameter coupling and a nonconvex loss landscape in nonlinear orthotropic inference, where the optimizer can traverse multiple basins before stabilizing.

In Table E.2, we report the inferred hyperparameters of the inverse-gamma distributions associated with v_s and σ^2 for the noise-free experiments. Despite the absence of added displacement noise, the posterior mean of σ^2 is on the order of 4.0×10^{-6}, which we attribute to residual numerical uncertainty in the forward and inference procedures. In contrast, the posterior mean of v_s is several orders of magnitude larger (approximately 4.1×10^6), indicating that, in this regime, uncertainty is predominantly governed by variability in the inferred material parameters rather than observational noise or numerical uncertainty.

4.2. Robustness to displacement noise: Gaussian white

We next assess robustness to displacement measurement noise by perturbing the measured full-field kinematics with additive Gaussian white noise at two levels, namely low ($\sigma_u = 1 \times 10^{-4}$ mm) and high ($\sigma_u = 1 \times 10^{-3}$ mm) [30–32,72]. No smoothing, stabilization, or displacement-field assimilation is applied prior to inference, such that the imposed perturbations act as a conservative stress test of the framework. We restrict attention to the geometrically heterogeneous training specimens, since these provided the most reliable baseline inference performance in the noise-free setting (Section 4.1).

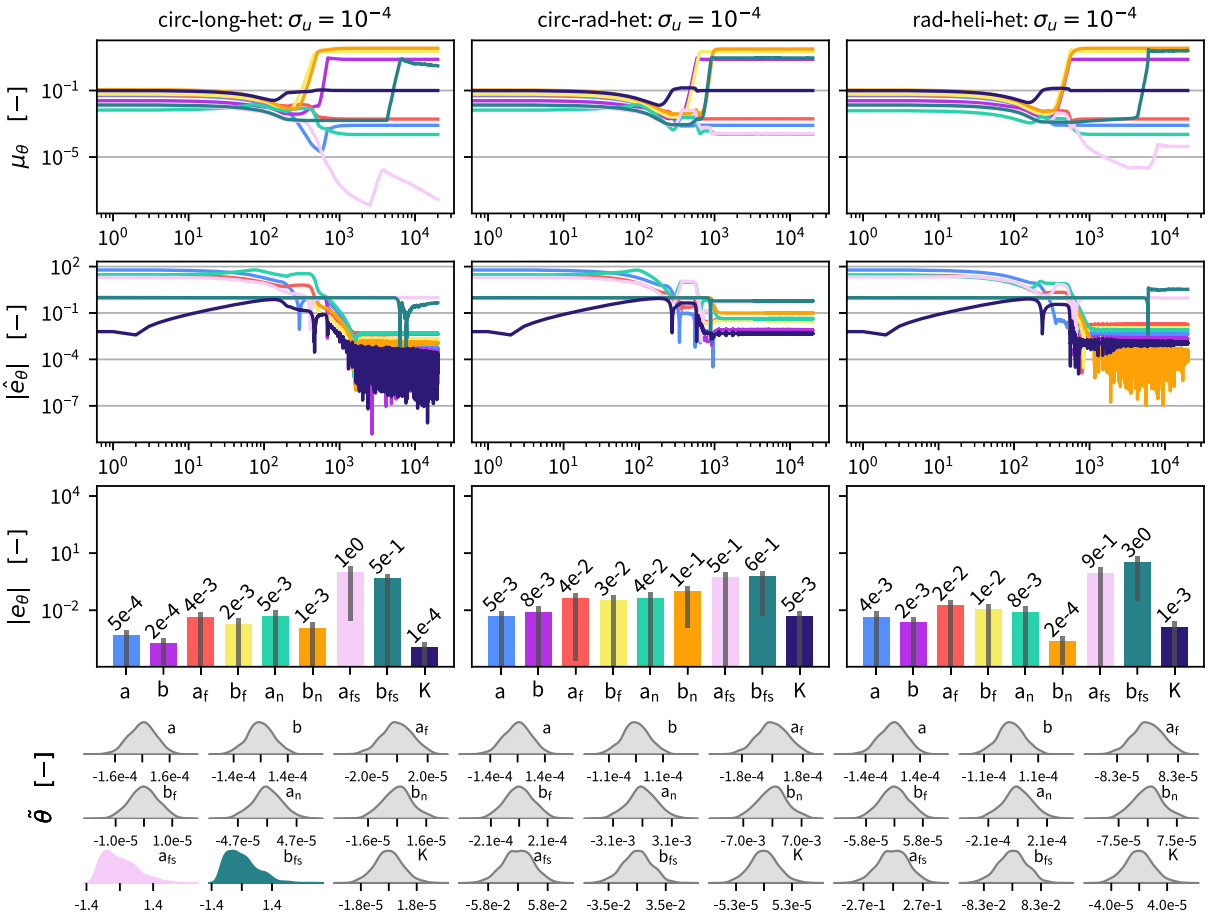

Fig. 8. Parameter inference on geometrically and microstructurally heterogeneous tissue slabs under low displacement measurement noise. From left to right: *circ-long-het*, *circ-rad-het*, and *rad-heli-het* specimens. From top to bottom: (i) evolution of inferred material parameters θ over optimization epochs, (ii) evolution of absolute relative location parameter errors $|\hat{e}_\theta|$, (iii) absolute relative errors $|e_\theta|$ at the final epoch with corresponding 95% credibility interval, and (iv) rescaled posterior distributions $\tilde{\theta}$ (drawn from the variational guide). The plots show that most parameters maintain stable convergence under low noise, while a_{fs} and b_{fs} exhibit the largest variability across specimens, reflected by slower convergence and broader posteriors. Here, uncorrelated Gaussian white displacement noise with standard deviation $\sigma_u = 10^{-4}$ mm is added to the full-field kinematics. Distributions are shown in grayscale when the absolute unbiased skewness satisfies $|s_{\tilde{\theta}}| < 0.5$. (For interpretation of the references to color in this figure legend, the reader is referred to the web version of this article.)

Fig. 8 summarizes inference under low displacement noise for the three geometrically heterogeneous training specimens. Across all three microstructural settings, the trajectories in rows (i) and (ii) indicate that the low-noise setting largely preserves the convergence patterns of the noise-free heterogeneous baseline in Fig. 7, and differences emerge most clearly in the shear-coupling terms. For *circ-long-het*, final relative errors for isotropic and primary anisotropic parameters stay within a narrow band, with representative values between 10^{-4} and 5×10^{-3} (Table F.8). In contrast, the parameter trajectory for a_{fs} does not settle to a clear plateau in row (i), and b_{fs} exhibits increased stochasticity together with a mild downward drift. The corresponding relative errors for the shear-coupling terms are of order one, with $|\hat{e}_{a_{fs}}| \approx 1$ and $|\hat{e}_{b_{fs}}| \approx 0.5$. This behavior is mirrored in the posterior samples in row (iv), which show pronounced skewness and visible truncation for (a_{fs}, b_{fs}), consistent with elevated uncertainty and weak practical identifiability under this noise level. Whereas in the noise-free heterogeneous setting (Fig. 7) the shear parameter a_{fs} could still be identified up to a relative error on the order of 10^{-2}, the low-noise case now produces errors for both a_{fs} and b_{fs} of the same order of magnitude as their true values. In the helically distributed fiber specimens *circ-rad-het* and *rad-heli-het*, the posterior samples in row (iv) do not exhibit comparable skewness or truncation for the inferred parameters. Compared with the noise-free case, the final relative errors for isotropic and primary anisotropic parameters are slightly higher, remaining mostly between 5×10^{-3} and 5×10^{-2} for *circ-rad-het* and between 3×10^{-4} and 5×10^{-2} for *rad-heli-het* (excluding a_{fs} and b_{fs}), while the majority of parameters still converge to clearly defined plateaus in rows (i) and (ii). For the shear-coupling terms, the posterior shapes of (a_{fs}, b_{fs}) become more regular in row (iv), yet their error traces in row (ii) plateau at comparatively elevated levels. In the noise-free case (Fig. 7), we achieved rotated-fiber shear-coupling errors $|\hat{e}_{a_{fs}}|$ of order 10^{-3} and $|\hat{e}_{b_{fs}}|$ of at most 10^{-3} in the *circ-rad-het* and *rad-heli-het* specimens (Table E.4). Under low noise here, these errors increase to magnitudes between roughly 5×10^{-1} and order one, with

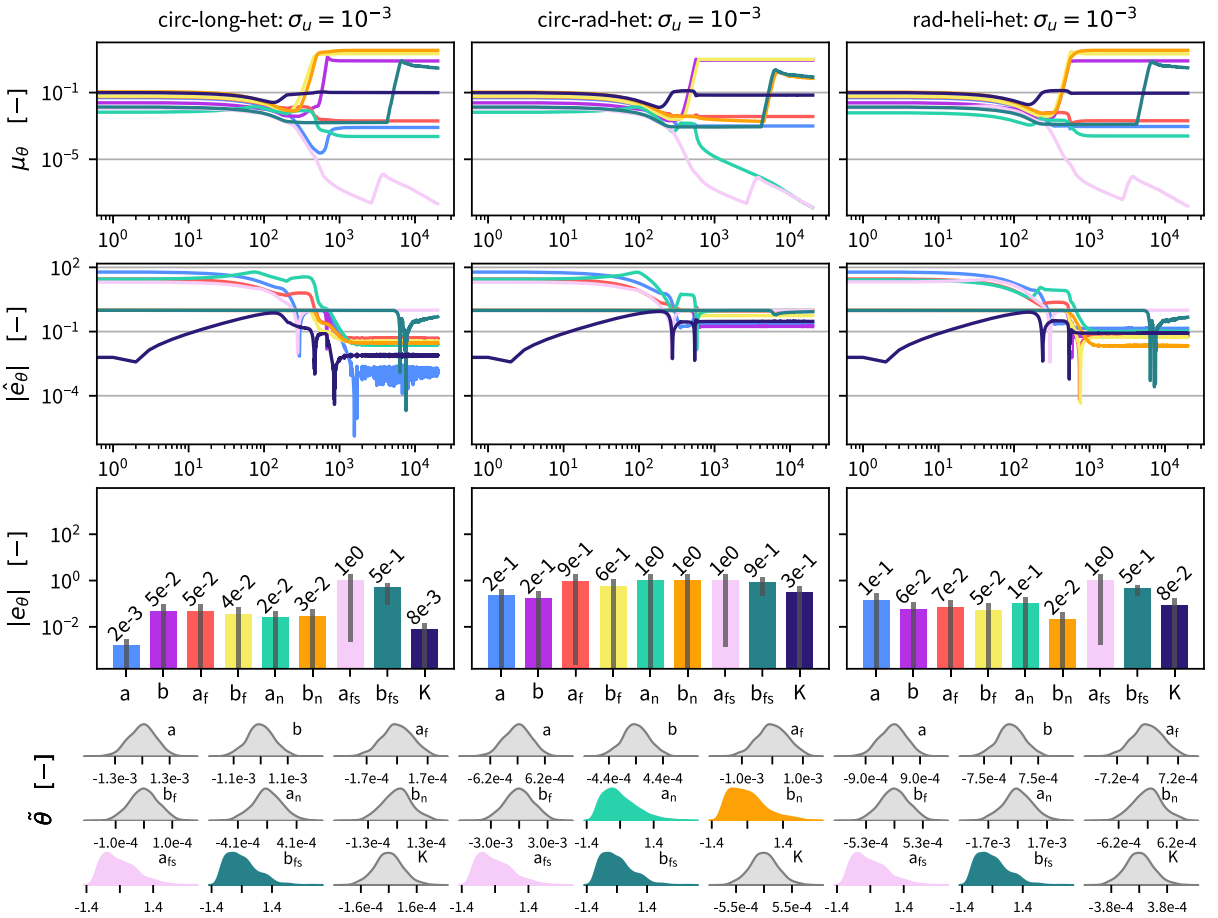

Fig. 9. Parameter inference on geometrically and microstructurally heterogeneous tissue slabs under high displacement measurement noise. From left to right: *circ-long-het*, *circ-rad-het*, and *rad-heli-het* specimens. From top to bottom: (i) evolution of inferred material parameters θ over optimization epochs, (ii) evolution of absolute relative location parameter errors $|\hat{e}_\theta|$, (iii) absolute relative errors $|e_\theta|$ at the final epoch with corresponding 95% credibility interval, and (iv) rescaled posterior distributions $\tilde{\theta}$ (drawn from the variational guide). The plots show increased variability and slower stabilization for several parameters compared with the low-noise case, with the shear-coupling parameters (a_{fs}, b_{fs}) exhibiting the largest spread in the posterior samples across specimens. Here, displacement noise with standard deviation $\sigma = 10^{-3}$ mm is added to the full-field kinematics. Distributions are shown in grayscale when the absolute unbiased skewness satisfies $|s_{\tilde{\theta}}| < 0.5$. (For interpretation of the references to color in this figure legend, the reader is referred to the web version of this article.)

the largest outlier observed for b_{fs} in *rad-heli-het* (Table F.8). Strikingly, the shear-coupling parameters stabilize in the *circ-rad-het* and *rad-heli-het* configurations after roughly 1000 and 10 000 epochs respectively, even though their relative errors remain high. Combined with the lack of skewness and truncation in their posteriors, this pattern is consistent with the parameters having moved away from the prior and having settled in a suboptimal local minimum under low-noise conditions.

Fig. 9 assesses parameter inference under high displacement measurement noise ($\sigma_u = 10^{-3}$ mm) for the three geometrically heterogeneous specimens, using the same layout as in Fig. 8. Relative to the low-noise case, the trajectories in rows (i) and (ii) show a marked loss of stability and accuracy, most prominently in the shear-coupling parameters (a_{fs}, b_{fs}). Across all three specimens, these shear terms no longer attain reliable plateaus, their estimates for a_{fs} collapse towards numerical near-zero values, and the corresponding relative errors remain of order one (Table F.8). In addition, the primary anisotropic sheet-direction parameters (a_n, b_n) in the *circ-rad-het* specimen fail to settle to stable values and reach relative errors close to unity, indicating a breakdown of identifiability in this parameter group under high noise. By contrast, the isotropic and primary anisotropic parameters remain comparatively more robust in *circ-long-het*, where final relative errors for these parameters mostly lie between 10^{-3} and 3×10^{-2}. In the *rad-heli-het* specimen, these relative parameter errors fall between 2×10^{-2} and 10^{-1} (Table F.8). The *circ-rad-het* configuration clearly performs worst overall, with many isotropic and primary anisotropic parameters exhibiting relative errors in the range 2×10^{-1} to 1, representing a sharp degradation compared with both the noise-free and low-noise cases. Similar to the low-noise setting, parameters that do stabilize under high noise typically do so around 1000 epochs for *circ-long-het*, *circ-rad-het*, and the *rad-heli-het*. Appendix F provides the corresponding noisy hyperparameter and constitutive parameter estimates, together with their relative errors and posterior scale parameters (Tables F.6–F.8), which quantitatively underpin the trends observed in Figs. 7–9.

Comparing Figs. 7, 8, and 9 show a clear, parameter-selective degradation of identifiability as displacement noise increases from zero to low to high levels. In the noise-free heterogeneous baseline (Fig. 7), isotropic and primary anisotropic parameters achieve small final deviations, with $|\hat{e}_\theta|$ typically below 5×10^{-4}, while the shear-coupling terms (a_{fs}, b_{fs}) are already more sensitive in *circ-long-het* but remain well identified in *circ-rad-het* and *rad-heli-het* (Table E.4). Under low noise (Fig. 8), these isotropic and primary anisotropic errors increase by roughly one to two orders of magnitude yet mostly remain below 10^{-1}, whereas the shear-coupling errors in *circ-long-het*, *circ-rad-het*, and *rad-heli-het* rise to order one or larger, consistent with the broadened and, in some cases, truncated posteriors for (a_{fs}, b_{fs}). At high noise (Fig. 9), this trend intensifies: the shear-coupling parameters lose practical identifiability in all three specimens, with $|\hat{e}_{a_{fs}}|$ and $|\hat{e}_{b_{fs}}|$ remaining of order one and the corresponding posterior samples strongly skewed, while selected primary anisotropic parameters in *circ-rad-het* (notably a_f, a_n, and b_n) also exhibit near-unity relative errors and non-stabilizing trajectories. By contrast, most isotropic parameters and the bulk modulus K retain comparatively moderate deviations even at the highest noise level, particularly in *circ-long-het* and *rad-heli-het*, indicating a degree of robustness in the volumetric and baseline stiffness sector despite the pronounced degradation in shear-related and directional anisotropic terms.

Table F.6 summarizes the inferred hyperparameters for experiments with additive Gaussian white displacement noise. For low noise levels ($\sigma_u = 10^{-4}$), the posterior mean of σ^2 increases to approximately 1.3×10^{-5}, while for higher noise levels ($\sigma_u = 10^{-3}$), it increases by roughly an order of magnitude. At the same time, the posterior mean of υ_s decreases from approximately 1.2×10^6 (low noise) to 1.1×10^5 (high noise). This trend indicates a progressive shift in the dominant source of uncertainty: as displacement noise increases, uncertainty associated with the likelihood (data noise) becomes more prominent relative to uncertainty attributed to the material model parameters.

4.3. Robustness to displacement noise: spatially correlated

We next consider an additional robustness study with spatially correlated displacement noise to further reflect the structured nature of experimental full-field measurement errors. Implementation details of the noise model are provided in Appendix B.

In Fig. 10, we assess parameter inference under a spatially correlated displacement noise field $\sigma_u(\mathbf{X})$ for the three geometrically heterogeneous specimens. The resulting degradation pattern is broadly similar to that observed under high Gaussian white noise, with the shear-coupling parameters (a_{fs}, b_{fs}) again showing the strongest loss of identifiability across all specimens. Most clearly, in the *circ-rad-het* specimen, the parameters (b_f, a_n, b_n) also degrade substantially, with relative errors of order of magnitude $\mathcal{O}(1)$. In the *rad-heli-het* specimen, b_n deteriorates similarly, whereas a_n still stabilizes but at a larger relative error of -1.516×10^1. In contrast, the *circ-long-het* specimen does not show additional parameter inference deterioration relative to the high Gaussian white-noise case, indicating that the impact of spatially correlated noise remains strongly specimen- and parameter-dependent. The posterior distributions in row (iv) reflect the same trend. Across all specimens, (a_{fs}, b_{fs}) retain the broadest uncertainty and, in several cases, also exhibit pronounced skewness, consistent with asymmetric and weak practical constraint under the structured noise perturbation. The *circ-rad-het* specimen additionally shows increased uncertainty in b_f, a_n, and b_n, while the *rad-heli-het* specimen shows a further broadening in b_n relative to the spatially uncorrelated Gaussian high-noise case. Overall, isotropic and primary anisotropic parameters that remain practically identifiable still tend to stabilize after roughly 10^3 epochs. In contrast, a_{fs} shows persistent drift towards numerically near-zero values, whereas b_{fs} converges only much later, around 1.7×10^4 epochs.

In Table G.10, we present the corresponding results for spatially correlated displacement noise. In this case, the posterior mean of σ^2 increases further to approximately 1.0×10^{-4}, representing an additional order-of-magnitude increase compared to the high Gaussian white noise setting. Concurrently, the posterior mean of υ_s decreases to $\mathcal{O}(10^4)$. Consistent with the previous observations, these results indicate a continued shift in the uncertainty structure, with the likelihood term increasingly dominating the overall uncertainty as both the magnitude and spatial complexity of the noise increase.

5. Validation beyond training

We now assess how well parameter sets inferred from single-shot heterogeneous biaxial tests generalize beyond the specific training protocol. To this end, we first compare Cauchy stress responses of 1000 parameter samples drawn from the inferred posterior under classical homogeneous uni-modal deformation modes against the ground-truth parameterized Holzapfel–Ogden law. Subsequently, we probe more complex mixed-modal deformation states, sampled from a physiologically constrained invariant space, and compare the resulting strain energy between 1000 parameter samples drawn from the inferred posterior and ground-truth parameters to assess generalization under heterogeneous load paths. Finally, in the following subsections we exclusively evaluate the isochoric parameter misfit of the strain–energy model (33) in order to ascertain internal consistency.

5.1. Uni-modal deformation mode validation

We reproduce homogeneous, uni-modal loading protocols, i.e. classical incompressible biaxial tension and triaxial shear tests, following the experimental protocols of [10,11]. We consider incompressible biaxial tension, where λ_f and λ_n are prescribed and λ_s follows from incompressibility, and triaxial shear tests, where the principal stretches are fixed to unity and a single shear component is activated per test. The resulting stress expressions are summarized in Appendix C. Constitutive parameters inferred from our unsupervised single-shot heterogeneous biaxial protocol are then used to assess, in a controlled fashion, the predictive capability of the proposed framework relative to established multi-modal calibration pipelines for myocardial tissue [12,15,16,26].

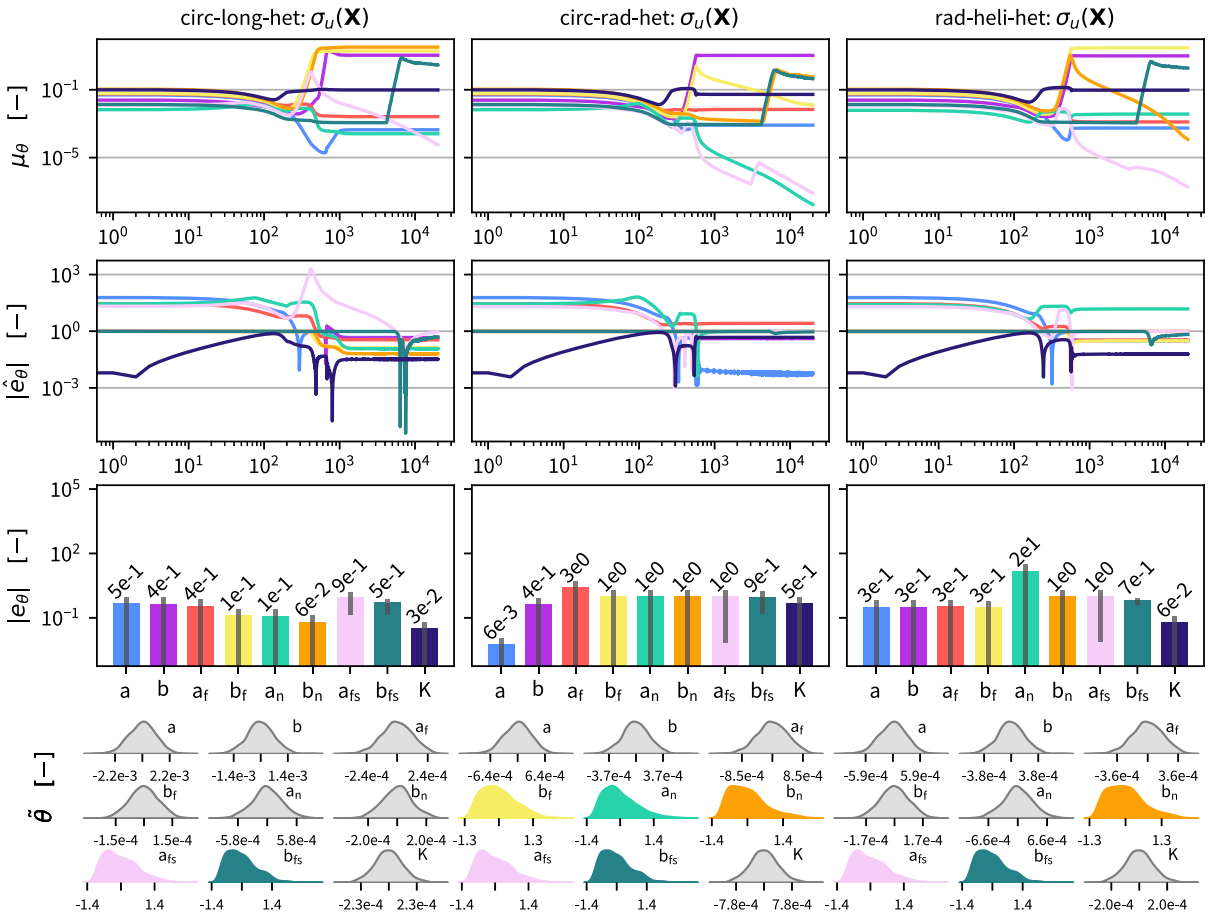

Fig. 10. Parameter inference on geometrically and microstructurally heterogeneous tissue slabs under spatially correlated displacement noise. From left to right: *circ-long-het*, *circ-rad-het*, and *rad-heli-het* specimens. From top to bottom: (i) evolution of inferred material parameters θ over optimization epochs, (ii) evolution of absolute relative location parameter errors $|\hat{e}_\theta|$, (iii) absolute relative errors $|e_\theta|$ at the final epoch with corresponding 95% credibility interval, and (iv) rescaled posterior distributions $\tilde{\theta}$ (drawn from the variational guide). Here, a spatially varying and spatially correlated displacement noise field $\sigma_u(\boldsymbol{X})$ is added to the full-field kinematics, as defined in Appendix B. The plots show increased variability and slower stabilization for several parameters, with the shear-coupling parameters (a_{fs}, b_{fs}) again exhibiting the strongest loss of identifiability across all specimens. Notably, the structured nature of the noise induces additional degradation in primary anisotropic parameters (such as b_f, a_n, and b_n) in the *circ-rad-het* and *rad-heli-het* specimens, while the *circ-long-het* specimen remains comparatively more robust. Distributions are shown in grayscale when the absolute unbiased skewness satisfies $|s_{\tilde{\theta}}| < 0.5$. (For interpretation of the references to color in this figure legend, the reader is referred to the web version of this article.)

Fig. 11 reports noise-free validation across the three geometrically heterogeneous configurations: *circ–long–het* (left), *circ–rad–het* (middle), and *rad–heli–het* (right). Each column compares Cauchy stresses from the ground-truth parameter set (tri markers) with predictions based on the noise-free single-shot full-field inference parameter sets (shaded 95% credible intervals) under classical biaxial tension and triaxial shear tests. Leveraging parameters inferred from the noise-free *circ-long–het* slab, the inferred biaxial stress–stretch curves match the ground-truth mechanical response of the tissue with $R^2 = 1.00$ for both biaxial tension cases. The inferred *nf*-, *sn*-, and *ns*-shear responses are also indistinguishable from the ground-truth response, whereas the inferred cross-fiber shear behavior shows lower agreement with respect to the ground-truth model, with $R^2 = 0.89$ and $R^2 = 0.77$ for σ_{fs} and σ_{sf} respectively. Aggregated over all tests in this configuration, the overall coefficient of determination amounts to $R^2 = 0.96$. These deviations are consistent with the limited deformational excitation of the I_{4fs} shear-coupling invariant in the *circ-long-het* specimen (Fig. 5) and with the weaker identifiability of (a_{fs}, b_{fs}) observed in the previous section. Leveraging the *circ-rad-het* slab, the inferred constitutive parameter sets perfectly reproduce the ground-truth stresses across all biaxial tension and shear tests with $R^2 = 1.00$ in every panel. Posterior confidence intervals remain tight, indicating precise recovery of the underlying constitutive parameters for this orientation, including the shear-coupling response. Focusing on the *rad-heli-het* specimen, the inferred stress curves again overlay the ground-truth for all biaxial tensile and shear tests with $R^2 = 1.00$. Overall, the noise-free within-model-class validation shows that single-shot full-field inference generalizes reliably across all three heterogeneous configurations, with slight deviations

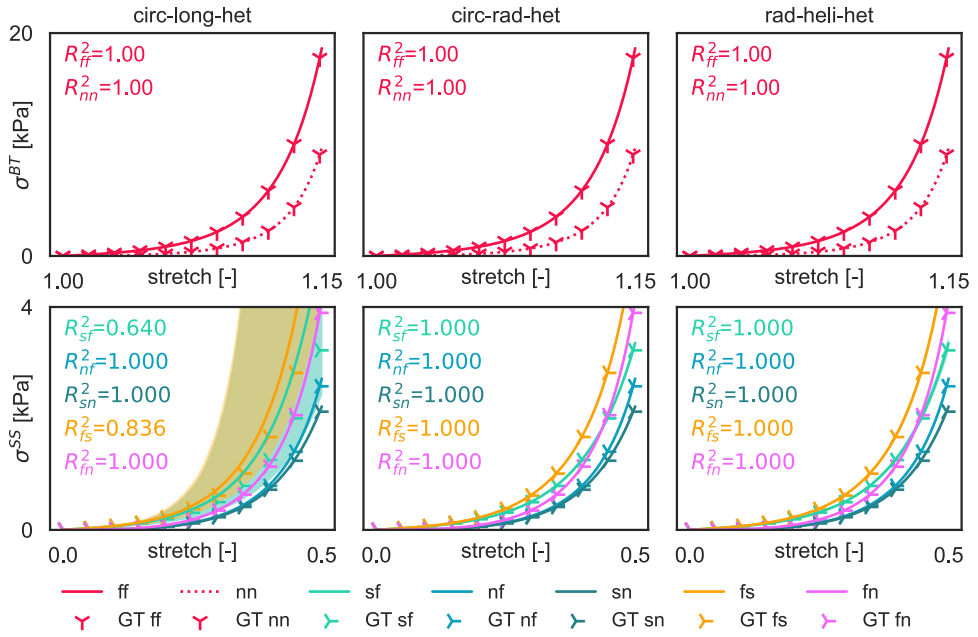

Fig. 11. Noise-free single-shot inference validation under homogeneous uni-modal loading. Cauchy stresses predicted by the ground-truth HO parameter set (tri markers) and by the inferred noise-free single-shot full-field posterior (shaded 95% credible intervals) for three heterogeneous configurations: *circ–long–het* (left), *circ–rad–het* (middle), and *rad–heli–het* (right). Rows correspond to classical incompressible biaxial tension and triaxial shear modes. Panel-wise R^2 values quantify agreement between posterior mean predictions and ground-truth stresses. Noise-free inference generalizes perfectly across all modes for *circ-rad-het* and *rad-heli-het* ($R^2 \approx 1$ throughout), while *circ-long-het* shows the largest deviations in cross-fiber shear (σ_{fs}, σ_{sf}). (For interpretation of the references to color in this figure legend, the reader is referred to the web version of this article.)

confined to cross-fiber shear in the *circ-long-het* case, which is in agreement with the parameter-level identifiability analysis in Fig. 7.

Fig. 12 reports high-noise ($\sigma_u = 10^{-3}$) validation for the same three heterogeneous single-shot slab specimens. Inferring from displacement and reaction force data in the *circ–long–het* specimen, the inferred biaxial tension behavior remains well aligned with the ground-truth, with panel-wise R^2 values close to one. Similarly, the *nf*-, *sn*-, and *ns*-shear responses retain correct magnitude and slope. Noise primarily affects the inferred cross-fiber shear stresses σ_{fs} and σ_{sf}, where credible intervals widen and small systematic deviations between ground-truth and inferred curves appear. Aggregated over all tests in this configuration, the overall coefficient of determination remains high at $R^2 = 0.96$. Leveraging the *circ–rad–het* slab, stresses computed from the high-noise inferred parameter sets no longer match the uni-modal ground-truth responses perfectly. Mean trends are preserved across biaxial and shear protocols, but panel-wise R^2 values are lower than in the *circ-long-het* and *rad-heli-het* configurations, particularly in cross-fiber and sheet-direction shear. Nevertheless, the aggregated coefficient of determination still reaches $R^2 = 0.73$. Lastly, we note the best uni-modal predictive nature of the inferred parameter set from the high-noise *rad-heli-het* specimen, with all panel-wise R^2-values greater than 0.87 and an aggregated coefficient of determination of $R^2 = 0.94$. Overall, at high displacement noise ($\sigma_u = 10^{-3}$) recovery of all HO-model parameters is no longer reliable as also reflected in the results in Section 4.2. Simultaneously, we observe that certain posterior-predictive quantities — specifically stress responses in selected loading modes — remain in reasonable agreement with the ground truth. The most notable of which are biaxial tension and non-cross-fiber triaxial shear. This indicates that, even when parameter identification breaks down, the inferred model can still provide informative predictions for specific deformation modes.

Lastly, Fig. 13 presents the uni-modal stress validation for the specimen-specific parameter sets inferred under spatially correlated displacement noise. For the *circ-long-het* specimen, the inferred biaxial tensile response remains well aligned with the ground truth, with panel-wise R^2 values close to one. We observe increased uncertainty in the σ_{fs} and σ_{sf} stresses, together with a slight mismatch in shear behavior. For the *circ-rad-het* specimen, the predictive behavior degrades compared to the high Gaussian white-noise case. The panel-wise R^2 values are lower than for *circ-long-het*, and now yield an aggregated coefficient of determination of $R^2 = 0.28$, mainly due to the mismatch in the (nf, sn, fn) shear directions. For the *rad-heli-het* specimen, performance also decreases, most clearly in the σ_{nn} and σ_{nf} directions, but it still attains an aggregated coefficient of determination of $R^2 = 0.86$.

5.2. Mixed-modal deformation validation

To probe generalization under mixed deformation modes, we sample deformation states in invariant spaces between the homogeneous loading paths. We draw $(I_1, I_{4ff}, I_{4nn}, I_{4fs})$ uniformly within the minimum and maximum values induced by the

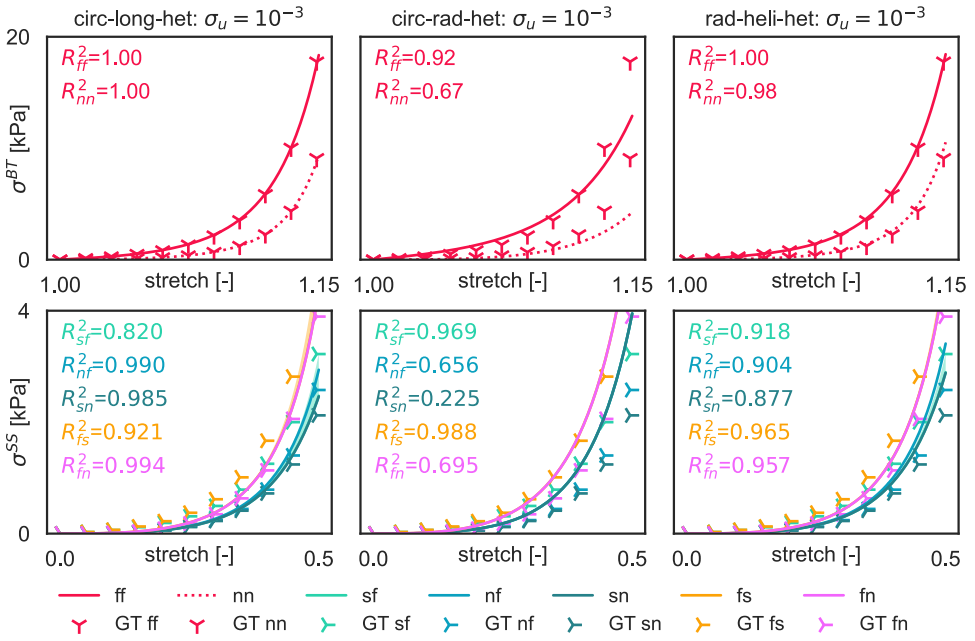

Fig. 12. High Gaussian white noise single-shot inference validation under homogeneous uni-modal loading. Cauchy stresses predicted by the ground-truth HO parameter set (tri markers) and by the inferred single-shot full-field posterior under Gaussian white displacement noise $\sigma_u = 10^{-3}$ mm (shaded 95% credible intervals) for *circ–long–het* (left), *circ–rad–het* (middle), and *rad–heli–het* (right). Rows correspond to the same biaxial tension and triaxial shear protocols as in Fig. 11. Panel-wise R^2 values quantify agreement between posterior mean predictions and ground-truth stresses. High noise primarily degrades cross-fiber shear predictivity and widens credible intervals, most notably for *circ-rad-het*, while biaxial tension and non-cross-fiber shear modes remain well captured, particularly for *circ-long-het* and *rad-heli-het*. (For interpretation of the references to color in this figure legend, the reader is referred to the web version of this article.)

homogeneous protocols in the uni-modal deformation, see also (C.1), and retain only physiologically admissible states. Specifically, we accept samples that satisfy near-incompressibility $0.9999 \leq J \leq 1.0001$ and whose maximum principal Cauchy stress does not exceed 20.3 kPa, consistent with reported peak stresses for left-ventricular biaxial tests on human myocardial tissue [11]. The invariant-to-kinematics reconstruction and stress evaluation used for filtering are detailed in Appendix D. We repeat this procedure until 5000 admissible mixed-modal states are obtained. Fig. 14 illustrates the resulting invariant coverage. The thin sweeping colored arcs represent the uni-modal loading conditions from the previous section, highlighting that these tests excite the invariants along low-dimensional paths. In contrast, our randomly sampled deformation gradients populate the space between these arcs and thus correspond to more complex mixed-modal testing protocols. The accepted samples lie between 3 and 3.25 in I_1, between 0.57 and 1.32 for I_{4ff} and I_{4nn}, and between −0.5 and 0.5 for I_{4fs}, and they are spread out approximately uniformly within this constrained region. This construction supports the view that the resulting invariant set spans a physiologically relevant range of deformation states that is well suited for out-of-training validation of the inferred versus ground-truth constitutive parameter set.

More specifically, we compute strain energies using both the ground-truth parameter set and the inferred parameter sets obtained from both low and high displacement measurement noise-affected heterogeneous training experiments. The correlation between the strain energy predicted by the inferred parameter sets Ψ and the ground truth Ψ^{GT} is shown as a hexbin plot in Fig. 15. The black diagonal centerline indicates optimal behavior, i.e. the inferred mechanical response matches the expected ground-truth response perfectly. In line with our prior results for the weakest identifiability of the noise-affected *circ-long–het* specimen in the parameter inference and uni-modal stress inference analysis, this specimen also yields the lowest strain–energy agreement across the multi-modal deformation modes with $R^2 = 0.91$ in the low-noise setting and $R^2 = 0.931$ in the high-noise setting. Across the three heterogeneous slabs tested, we observe larger deviations away from the diagonal, indicating that a subset of randomly sampled invariant combinations, together with corresponding posterior samples, lead to strain energies that differ more strongly from the ground-truth. The *circ-rad-het* specimen shows a very high coefficient of determination in the low-noise case ($R^2 = 0.989$), and its performance slightly degrades to $R^2 = 0.915$ in the high-noise case. Despite this drop, *circ-rad-het* exhibits the tightest clustering of hexbin intensities around the diagonal, suggesting that most mixed-modal states are still well captured, with a relatively small number of outliers contributing to the R^2 reduction. Lastly, the most consistent performing sample is the *rad-heli-het* with an R^2 score of 0.962 in the low noise setting and 0.968 in the high noise setting.

Overall, the mixed-modal strain–energy validation indicates that, even though high displacement noise can substantially perturb individual parameter estimates — particularly the shear-coupling and some directional anisotropic terms — the inferred models retain strong predictive capability at the level of strain energy across a broad set of physiologically admissible deformation states

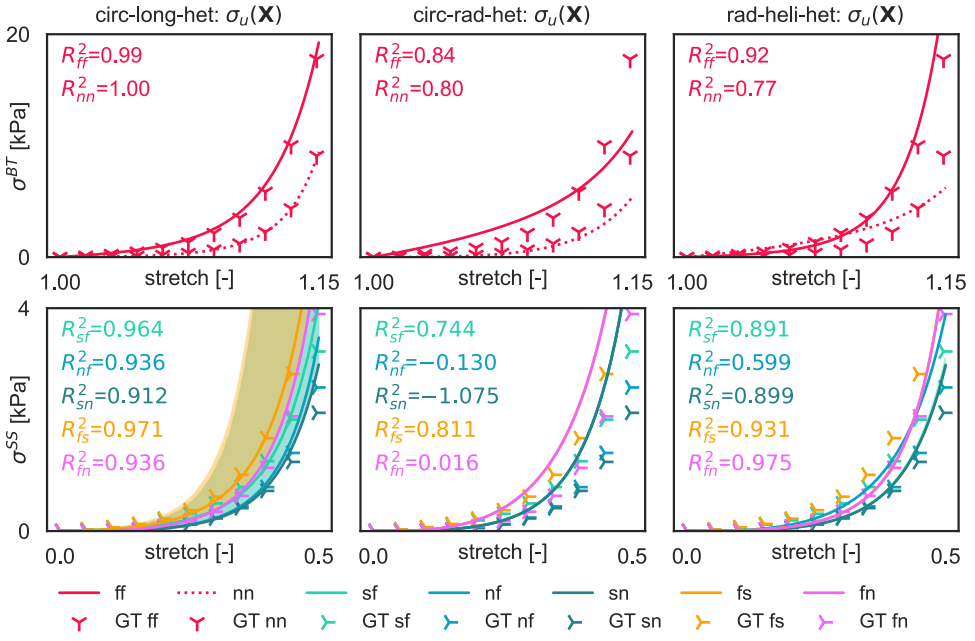

Fig. 13. Spatially correlated noise single-shot inference validation under homogeneous uni-modal loading. Cauchy stresses predicted by the ground-truth HO parameter set (tri markers) and by the inferred single-shot full-field posterior under displacement noise $\sigma_u(\boldsymbol{X})$ (shaded 95% credible intervals) for *circ–long–het* (left), *circ–rad–het* (middle), and *rad–heli–het* (right). Rows correspond to the same biaxial tension and triaxial shear protocols as in Fig. 11. Panel-wise R^2 values quantify agreement between posterior mean predictions and ground-truth stresses. Spatially correlated noise mainly introduces larger posterior stress uncertainty in the *circ-long-het* sample. It further introduces a mismatch in n-directional stress in biaxial tension for the *circ-rad-het* and *rad-heli-het* samples. (For interpretation of the references to color in this figure legend, the reader is referred to the web version of this article.)

(all $R^2 \geq 0.9$). This finding complements the stress-based validation and suggests that the proposed single-shot full-field identification framework can retain strong predictive accuracy beyond the specific training protocol, provided that geometric and microstructural heterogeneity are sufficiently rich and measurement noise remains within a moderate range.

6. Discussion

The ability to infer complex orthotropic hyperelastic models from a single full-field biaxial tensile testing experiment represents an interesting avenue in biomechanical tissue characterization. Conventional constitutive identification workflows for complex orthotropic tissues such as the myocardium, typically rely on assumed microstructural homogeneity across the tissue specimen and leverage multiple specialized uni-modal loading protocols to identify constitutive parameter sets [10,11,73]. This reflects a broader challenge in calibrating orthotropic HO laws for the myocardium: parameter uniqueness is generally difficult to guarantee under limited excitation, motivating multi-modal protocols, sensitivity-informed reparameterizations, or model reduction [15,74–76] This work demonstrates that a single heterogeneous biaxial experiment, when combined with full-field kinematics and sparse reaction-force measurements, can support uncertainty-aware inference of a nonlinear orthotropic Holzapfel–Ogden (HO) parameter set using stochastic variational inference. Beyond the identifiability perspective, this single-shot strategy reduces experimental tissue manipulation and is particularly attractive for heterogeneous biological tissues, where sample availability or repeat testing is limited. Across the considered slab configurations, two consistent findings emerge: (i) identifiability is primarily governed by the degree to which the experiment excites the relevant invariant subspace, and (ii) even when individual HO parameters are not recovered accurately under varying levels of displacement measurement noise, the inferred models can remain highly predictive for stresses and strain energy over both uni-modal and mixed-modal deformation states. These observations clarify when single-shot full-field inference can be expected to recover the full parameter set, and when it should instead be interpreted as delivering a reliable posterior predictive constitutive response with quantified uncertainty.

Heterogeneity as an experimental design principle for orthotropic constitutive parameter inference. Dominant gains in constitutive parameter identifiability arise from deliberately enriching the deformation space within a single test. Microstructural heterogeneity, introduced through slab orientation and the associated transmural fiber rotation, and geometric heterogeneity, introduced through a central occlusion, both broaden the activated distributions of I_1, I_{4ff}, I_{4nn}, and I_{4fs} (Figs. 4–5). These experimental protocol choices increase the sensitivity of the equilibrium residuals to the full parameter vector $\boldsymbol{\theta}$. In the noise-free setting, this explains the contrast between homogeneous and heterogeneous specimens in Figs. 6–7. Most isotropic and

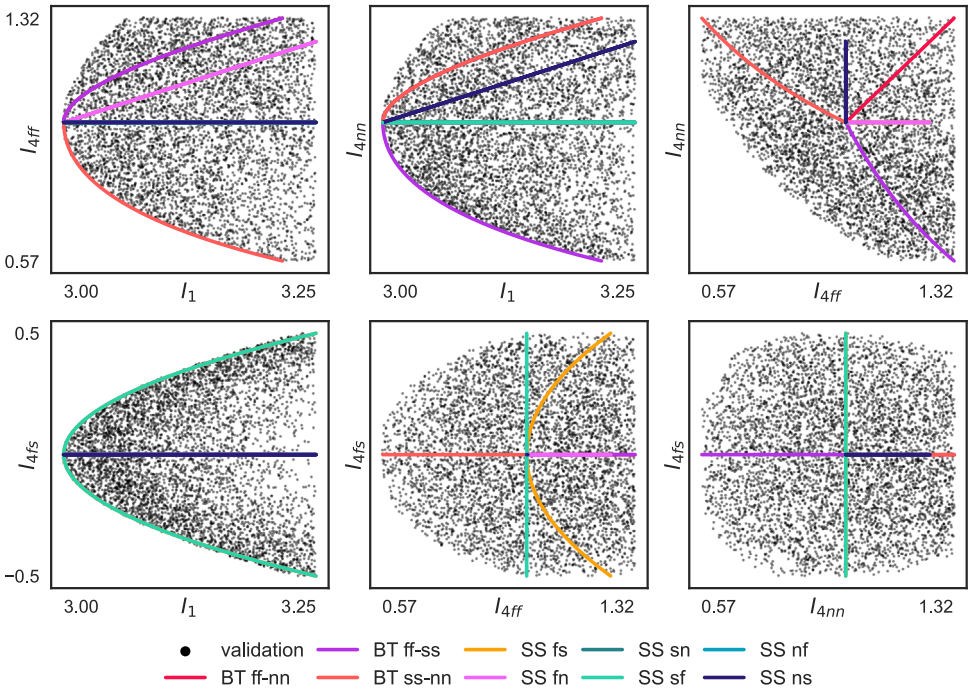

Fig. 14. Mixed-modal validation set construction in invariant space. Invariant trajectories induced by uni-modal biaxial and single-shear protocols (colored curves) compared with randomly sampled invariant combinations that satisfy (quasi-)incompressibility and a physiological bound on maximum principal stress detailed in Appendix D. The uni-modal protocols excite low-dimensional paths, whereas the accepted multi-modal deformation modes populate the space between these uni-modal paths, yielding mixed-modal deformation states for further and richer out-of-training validation. (For interpretation of the references to color in this figure legend, the reader is referred to the web version of this article.)

primary anisotropic parameters are inferred robustly across configurations, while the shear-coupling parameters (a_{fs}, b_{fs}) become practically identifiable only when the single slab biaxial tension experiment produces appreciable I_{4fs} excitation. The *circ-rad-het* and *rad-heli-het* slab configurations provide the most consistent recovery of these terms, reflecting the combined effect of geometry-induced strain gradients and orientation-driven multiaxial activation of the microstructure. In this sense, our results translate the multi-modal calibration message from prior myocardium studies into a single-shot setting: rather than combining separate stretch and shear protocols, we aim to excite the same (otherwise weakly constrained) coupling modes within one heterogeneous experiment [10,11,15]. These results further suggest that future protocols could deliberately combine geometrical and microstructural tailoring to maximize parameter observability within a single specimen.

Experimental displacement measurement noise selectively impacts constitutive parameter identifiability. Displacement noise degrades constitutive parameter identifiability selectively rather than uniformly. For low noise ($\sigma_u = 10^{-4}$ mm), Fig. 8 shows stable convergence and comparatively narrow posteriors for the isotropic and primary anisotropic parameters. In contrast, (a_{fs}, b_{fs}) show the largest posterior broadening and, in some cases, pronounced skewness or truncation of the inferred posterior parameter distribution. For high noise ($\sigma_u = 10^{-3}$ mm), Fig. 9 showcases how the shear-coupling terms lose practical identifiability across specimens, and additional degradation can appear in directional anisotropic parameters, most clearly in *circ-rad-het*. These results are consistent with global sensitivity and inverse uncertainty quantification studies of the underlying Holzapfel-Ogden constitutive model [43,76,77], which show that parameter sensitivity and practical identifiability depend strongly on the deformation modes and invariant support represented in the available data. Two implications follow. Full-field single-shot inference strongly benefits from experimental designs that amplify invariants associated with weaker energy modes. In addition, posterior-shape diagnostics such as truncation and skewness provide useful indicators of noise-driven practical non-identifiability and should be interpreted alongside point estimates.

Identifiability versus predictive capability. An important result is that imperfect recovery of ground-truth HO parameters does not necessarily imply poor constitutive prediction, as also noted in prior HO calibration and in vivo estimation studies [26,74]. Figs. 11–12 show that posterior predictive stresses under classical homogeneous uni-modal protocols remain accurate in aggregate, even at high noise. Fig. 15 shows strong strain–energy correlation across 5000 physiologically admissible mixed-modal deformation states, with all $R^2 \geq 0.9$. When viewed together with the parameter-level degradation in Figs. 8–9, these results indicate that distinct parameter combinations can yield near-indistinguishable macroscopic responses over the rich explored invariant deformation space [15,76]. In such cases, the posterior predictive response, together with its credible interval, becomes more relevant for

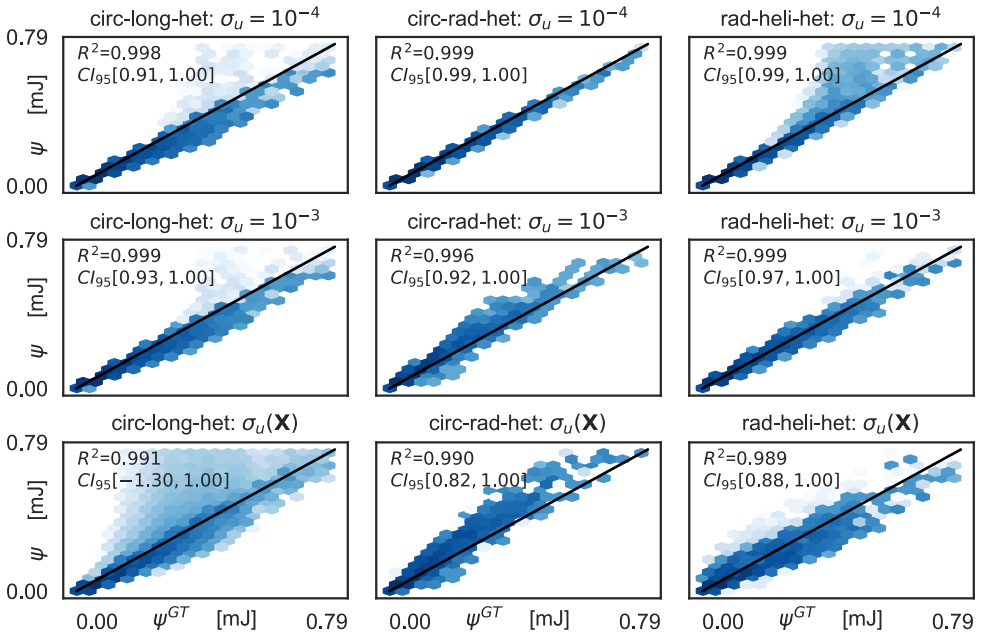

Fig. 15. Strain–energy generalization under mixed-modal deformations. Correlation between strain energy predicted by inferred parameter posteriors, Ψ, and the ground-truth strain energy, Ψ^{GT}, over 5000 accepted mixed-modal deformation states sampled in invariant space (Fig. 14). Results are shown for geometrically heterogeneous training specimens under low and high displacement measurement noise, i.e. $\sigma_u = 10^{-4}$ and 10^{-3} mm respectively, as well as for spatially correlated noise. Hexbin density emphasizes the dominant response region, and the black diagonal indicates perfect agreement. Despite noise-driven degradation of select parameter groups, predicted energies remain strongly correlated with the ground-truth across mixed-modal states (all $R^2 \geq 0.9$). The 95% confidence interval shows degrading scores as the noise level increases and as spatially correlated noise is added. Note that R^2 denotes the median score for all samples from the posterior.

downstream simulation than any single best-fit parameter vector and is consistent with inference perspectives that emphasize parameter distributions rather than unique point estimates [32,35,41,78]. This perspective is particularly pertinent for soft tissues, where measurement noise, limited loading diversity, and intrinsic variability constrain practical identifiability.

Some heterogeneous configurations remain more predictive under noise. Our validation results also reveal slab-specific trends. The *circ-rad-het* configuration can be more sensitive to displacement noise in the uni-modal and mixed-modal validations, despite exhibiting a rich heterogeneous deformation profile in Fig. 5. This observation indicates that heterogeneity alone is not sufficient. Identifiability also depends on how displacement measurement noise perturbs the invariants that control weaker energy modes and how these perturbations propagate through the equilibrium residuals, which is consistent with the broader observation that the subset of HO terms supported by data depends on the deformation modes represented in the calibration dataset [15]. In contrast, *rad-heli-het* exhibits the most consistent predictive performance across stress and energy validations in Figs. 11–15, making it a promising slicing orientation when a single-shot protocol is prioritized and robust in-plane excitation of multiple microstructural constituent contributions is feasible.

Outlook. The present findings should be interpreted as a controlled identifiability and robustness study rather than as a full experimental validation of the workflow. By construction, the synthetic setting assumes known boundary conditions, known microstructural fields, thin slices, and an *a priori* Holzapfel–Ogden model form, which allows us to isolate how heterogeneity, model nonlinearity, and displacement noise affect inference performance. From an inverse-identification perspective, the chosen slab thickness is conservative, since thicker specimens would in principle provide more internal kinematic information if measured reliably. Our noise studies should likewise be interpreted as deliberately conservative robustness tests. We intentionally did not apply smoothing, stabilization, or displacement-field assimilation prior to inference. We instead first considered spatially uncorrelated Gaussian white noise as a coarse worst-case perturbation of the full-field kinematics, with noise magnitudes chosen in line with prior inverse and Bayesian identification studies [30–32,72]. At the same time, realistic full-field displacement measurements are typically more structured, with spatial correlations and degradation near boundaries and interfaces. The added spatially correlated noise study therefore represents a first step towards a more experimentally realistic setting. Nevertheless, it remains an idealized robustness test rather than a complete model of DIC/DVC measurement error [29,79]. From an experimental perspective, these results suggest that successful application will depend not only on sufficiently rich invariant excitation within a single specimen, but also on careful treatment of boundary-condition uncertainty, missing near-boundary data, uncertainty or misregistration in the measured microstructural fields, and model form discrepancy. Automated model discovery frameworks provide an interesting avenue to address both practical non-identifiability and model form discrepancy in settings with complex loading patterns and

varying amounts of measurement noise [16,30,32,33,53,80]. Complementary directions include explicit probabilistic models for displacement measurement error, experimental designs that target weakly activated invariants, and alternative variational weighting strategies to improve robustness under noisy full-field data [29,79,81]. Variational families that capture posterior dependencies more accurately, combined with posterior predictive checks tailored to equilibrium residuals, would further strengthen uncertainty quantification. Finally, the present study focused on spatially homogeneous material parameters with spatially varying structure fields. Extending the framework to spatially varying parameter fields with appropriate regularization could be valuable for truly heterogeneous tissues, while raising additional identifiability and experimental design challenges [82,83]. Overall, our results support single-shot, uncertainty-aware identification of nonlinear orthotropic constitutive behavior from a single heterogeneous biaxial test. Our main experimental design message is that the relevant invariant subspace must be sufficiently activated, with particular emphasis on the weak shear-coupling mode. At the same time, the validation results show that posterior predictive accuracy can remain high even when individual parameters are poorly identifiable due to noise.

7. Conclusion

We presented a physics-informed stochastic variational framework that recovers the full constitutive parameter set of a nonlinear orthotropic hyperelastic model from a single biaxial stretch experiment. By exploiting intrinsic microstructural heterogeneity, or introducing simple geometric heterogeneity when needed, the method identifies not only the dominant tensile parameters but also shear-coupling terms that are typically weakly excited in biaxial tension. Our results demonstrate that an effective balance between the underlying microstructure and biaxial loading improves identifiability, and that this balance can be set through slicing and tissue harvesting. Circumferential–radial slabs and rotated cuts that place both fiber and sheet directions in the loading plane enable the recovery of the full parameter set under noise-free conditions. Under realistic yet spatially stationary, displacement measurement noise levels, our framework yields stress responses and strain energies in close agreement with the ground-truth mechanical response and provides posterior uncertainty estimates for the underlying constitutive parameters. Isotropic and primary anisotropic parameters are generally robust, whereas shear-coupling parameters and selected sheet-direction terms are more susceptible to degradation under displacement noise, particularly for spatially varying and boundary amplified perturbation. Adding geometric heterogeneity, such as a central occlusion, systematically improves convergence and tightens posterior distributions, especially for shear-coupling parameters. These results indicate that slicing protocols and experimental design can be used deliberately to enhance observability in full-field inverse characterization. More broadly, the framework enables localized characterization of orthotropic nonlinear biological tissues from a single heterogeneous full-field experiment. As such, this work provides a controlled but important first step towards translating single-shot, uncertainty-aware constitutive inference to real full-field tissue experiments. This reduces experimental tissue manipulation, improves reproducibility, and supports studies where available tissue is limited.

CRediT authorship contribution statement

Rogier P. Krijnen: Writing – review & editing, Writing – original draft, Visualization, Validation, Software, Methodology, Investigation, Conceptualization. **Akshay Joshi:** Writing – review & editing, Methodology. **Siddhant Kumar:** Writing – review & editing, Supervision, Methodology. **Mathias Peirlinck:** Writing – review & editing, Writing – original draft, Supervision, Resources, Project administration, Methodology, Investigation, Funding acquisition, Formal analysis, Conceptualization.

Declaration of competing interest

The authors declare that they have no known competing financial interests or personal relationships that could have appeared to influence the work reported in this paper.

Acknowledgments

This work was supported by the Dutch Research Council (NWO) through the NWO Veni Talent Program, project number 20058, awarded to Mathias Peirlinck.

Supplementary data

Supplementary material related to this article can be found online at https://doi.org/10.1016/j.cma.2026.119034.

Data availability

Data will be made available on request. Lab codes are published on github.com/peirlincklab.

References

[1] M. Peirlinck, F.S. Costabal, J. Yao, J.M. Guccione, S. Tripathy, Y. Wang, D. Ozturk, P. Segars, T.M. Morrison, S. Levine, E. Kuhl, Precision medicine in human heart modeling: Perspectives, challenges, and opportunities, Biomech. Model. Mechanobiol. 20 (3) (2021) 803–831, http://dx.doi.org/10.1007/s10237-021-01421-z.

[2] S.A. Niederer, K.S. Campbell, S.G. Campbell, A short history of the development of mathematical models of cardiac mechanics, J. Mol. Cell. Cardiol. (2019) http://dx.doi.org/10.1016/j.yjmcc.2018.11.015.

[3] C. Reeps, A. Maier, J. Pelisek, F. Härtl, V. Grabher-Meier, W.A. Wall, M. Essler, H.-H. Eckstein, M.W. Gee, Measuring and modeling patient-specific distributions of material properties in abdominal aortic aneurysm wall, Biomech. Model. Mechanobiol. 12 (4) (2012) 717–733, http://dx.doi.org/10.1007/s10237-012-0436-1.

[4] S. Roccabianca, C.A. Figueroa, G. Tellides, J.D. Humphrey, Quantification of regional differences in aortic stiffness in the aging human, J. Mech. Behav. Biomed. Mater. 29 (2014) 618–634, http://dx.doi.org/10.1016/j.jmbbm.2013.01.026.

[5] S. Budday, G. Sommer, C. Birkl, C. Langkammer, J. Haybaeck, J. Kohnert, M. Bauer, F. Paulsen, P. Steinmann, E. Kuhl, G.A. Holzapfel, Mechanical characterization of human brain tissue, Acta Biomater. 48 (2017) 319–340, http://dx.doi.org/10.1016/j.actbio.2016.10.036.

[6] K. Matouš, M.G.D. Geers, V.G. Kouznetsova, A. Gillman, A review of predictive nonlinear theories for multiscale modeling of heterogeneous materials, J. Comput. Phys. 330 (2017) 192–220, http://dx.doi.org/10.1016/j.jcp.2016.10.070.

[7] N. Famaey, H. Fehervary, Y. Lafon, A. Akyildiz, S. Dreesen, K. Bruyère-Garnier, J.-M. Allain, M. Alloisio, A. Aparici-Gil, C. Catalano, F. Chassagne, S. Chokhandre, K. Crevits, H. Crielaard, E. Cunnane, C. Cunnane, K. De Leener, A. Desai, R. Driessen, A. Erdemir, M. Eskandari, S. Evans, C. Gasser, M. Gebhardt, B. Glasmacher, G.A. Holzapfel, M. Isasi, L. Jennings, S. Kurz, S. Leal-Marin, P. Lecomte, A. Morch, J. Mulvihill, F. Nemavhola, T. Pandelani, S. Pasta, E. Peña, B. Pierrat, H.-L. Ploeg, S. Polzer, M. Rausch, D. Schwarz, H. Screen, S. Sherifova, G. Sommer, S. Wang, D. Walsh, D. Yadav, T. Marchal, L. Geris, Community challenge towards consensus on characterization of biological tissue: C4Bio's first findings, J. Biomech. (2026) http://dx.doi.org/10.1016/j.jbiomech.2025.113021.

[8] D. Rohmer, A. Sitek, G.T. Gullberg, Reconstruction and visualization of fiber and laminar structure in the normal human heart from ex vivo diffusion tensor magnetic resonance imaging (DTMRI) data, Invest. Radiol. 42 (11) (2007) 777, http://dx.doi.org/10.1097/RLI.0b013e3181238330.

[9] D.B.E. Alexander J. Wilson, Myocardial mesostructure and mesofunction, 2022, http://dx.doi.org/10.1152/ajpheart.00059.2022.

[10] S. Dokos, B.H. Smaill, A.A. Young, I.J. LeGrice, Shear properties of passive ventricular myocardium, Am. J. Physiol.-Heart Circ. Physiol. 283 (6) (2002) H2650–H2659, http://dx.doi.org/10.1152/ajpheart.00111.2002.

[11] G. Sommer, A.J. Schriefl, M. Andrä, M. Sacherer, C. Viertler, H. Wolinski, G.A. Holzapfel, Biomechanical properties and microstructure of human ventricular myocardium, Acta Biomater. 24 (2015) 172–192, http://dx.doi.org/10.1016/j.actbio.2015.06.031.

[12] S. Kakaletsis, W.D. Meador, M. Mathur, G.P. Sugerman, T. Jazwiec, M. Malinowski, E. Lejeune, T.A. Timek, M.K. Rausch, Right ventricular myocardial mechanics: Multi-modal deformation, microstructure, modeling, and comparison to the left ventricle, Acta Biomater. 123 (2021) 154–166, http://dx.doi.org/10.1016/j.actbio.2020.12.006.

[13] B. Staber, J. Guilleminot, Stochastic hyperelastic constitutive laws and identification procedure for soft biological tissues with intrinsic variability, J. Mech. Behav. Biomed. Mater. 65 (2017) 743–752, http://dx.doi.org/10.1016/j.jmbbm.2016.09.022.

[14] G.A. Holzapfel, R.W. Ogden, Constitutive modelling of passive myocardium: a structurally based framework for material characterization, Philos. Trans. R. Soc. A 367 (1902) (2009) 3445–3475, http://dx.doi.org/10.1098/rsta.2009.0091.

[15] D. Guan, F. Ahmad, P. Theobald, S. Soe, X. Luo, H. Gao, On the AIC-based model reduction for the general Holzapfel–Ogden myocardial constitutive law, Biomech. Model. Mechanobiol. 18 (4) (2018) 1213–1232, http://dx.doi.org/10.1007/s10237-019-01140-6.

[16] D. Martonová, M. Peirlinck, K. Linka, G.A. Holzapfel, S. Leyendecker, E. Kuhl, Automated model discovery for human cardiac tissue: Discovering the best model and parameters, Comput. Methods Appl. Mech. Engrg. 428 (2024) 117078, http://dx.doi.org/10.1016/j.cma.2024.117078.

[17] H. Fehervary, M. Smoljkić, J. Vander Sloten, N. Famaey, Planar Biaxial Testing of Soft Biological Tissues (Ph.D. thesis), KU Leuven, 2018.

[18] M. Alloisio, J.J.M. Wolffs, T.C. Gasser, Specimen width affects vascular tissue integrity for in-vitro characterisation, J. Mech. Behav. Biomed. Mater. 154 (2024) 106520, http://dx.doi.org/10.1016/j.jmbbm.2024.106520.

[19] T. Vervenne, N. Vermeeren, N. Demeersseman, H. Fehervary, M. Peirlinck, E. Kuhl, N. Famaey, Stretching the limits: From Planar-Biaxial Stress–Stretch to arterial pressure–diameter, J. Biomech. Eng. (2026) http://dx.doi.org/10.1115/1.4070124.

[20] Z. Wang, J.B. Estrada, E.M. Arruda, K. Garikipati, Inference of deformation mechanisms and constitutive response of soft material surrogates of biological tissue by full-field characterization and data-driven variational system identification, J. Mech. Phys. Solids 153 (2021) 104474, http://dx.doi.org/10.1016/j.jmps.2021.104474.

[21] C. Jailin, A. Benady, R. Legroux, E. Baranger, Experimental learning of a hyperelastic behavior with a Physics-Augmented neural network, Exp. Mech. 64 (9) (2024) 1465–1481, http://dx.doi.org/10.1007/s11340-024-01106-5.

[22] S. Meng, A.A.K. Yousefi, S. Avril, Machine-learning-based virtual fields method: Application to anisotropic hyperelasticity, Comput. Methods Appl. Mech. Engrg. 434 (2025) 117580, http://dx.doi.org/10.1016/j.cma.2024.117580.

[23] M. Grédiac, F. Pierron, S. Avril, E. Toussaint, The virtual fields method for extracting constitutive parameters from Full-Field measurements: a review, Strain 42 (4) (2006) 233–253, http://dx.doi.org/10.1111/j.1475-1305.2006.tb01504.x.

[24] F. Pierron, M. Grédiac, The Virtual Fields Method: Extracting Constitutive Mechanical Parameters from Full-field Deformation Measurements, Springer New York, 2012, http://dx.doi.org/10.1007/978-1-4614-1824-5.

[25] K.T. Kavanagh, R.W. Clough, Finite element applications in the characterization of elastic solids, Int. J. Solids Struct. 7 (1) (1971) 11–23, http://dx.doi.org/10.1016/0020-7683(71)90015-1.

[26] M. Peirlinck, K.L. Sack, P. De Backer, P. Morais, P. Segers, T. Franz, M. De Beule, Kinematic boundary conditions substantially impact in silico ventricular function, Int. J. Numer. Methods Biomed. Eng. 35 (1) (2018) http://dx.doi.org/10.1002/cnm.3151.

[27] A. Elouneg, D. Sutula, J. Chambert, A. Lejeune, S.P.A. Bordas, E. Jacquet, An open-source FEniCS-based framework for hyperelastic parameter estimation from noisy full-field data: Application to heterogeneous soft tissues, Comput. Struct. 255 (2021) 106620, http://dx.doi.org/10.1016/j.compstruc.2021.106620.

[28] D. Claire, F. Hild, S. Roux, A finite element formulation to identify damage fields: the equilibrium gap method, Internat. J. Numer. Methods Engrg. 61 (2) (2004) 189–208, http://dx.doi.org/10.1002/nme.1057.

[29] A. Peyraut, M. Genet, Finite strain formulation of the discrete equilibrium gap principle: application to direct parameter estimation from large full-fields measurements, C. R. Méc. 353 (G1) (2025) 259–309, http://dx.doi.org/10.5802/crmeca.279.

[30] M. Flaschel, S. Kumar, L. De Lorenzis, Unsupervised discovery of interpretable hyperelastic constitutive laws, Comput. Methods Appl. Mech. Engrg. 381 (2021) 113852, http://dx.doi.org/10.1016/j.cma.2021.113852.

[31] P. Thakolkaran, A. Joshi, Y. Zheng, M. Flaschel, L. De Lorenzis, S. Kumar, NN-EUCLID: Deep-learning hyperelasticity without stress data, J. Mech. Phys. Solids 169 (July) (2022) 105076, http://dx.doi.org/10.1016/j.jmps.2022.105076.

[32] A. Joshi, P. Thakolkaran, Y. Zheng, M. Escande, M. Flaschel, L. De Lorenzis, S. Kumar, Bayesian-EUCLID: Discovering hyperelastic material laws with uncertainties, Comput. Methods Appl. Mech. Engrg. 398 (2022) 115225, http://dx.doi.org/10.1016/j.cma.2022.115225.

[33] P. Thakolkaran, Y. Guo, S. Saini, M. Peirlinck, B. Alheit, S. Kumar, Can KAN CANs? Input-convex Kolmogorov-Arnold Networks (KANs) as hyperelastic constitutive artificial neural networks (CANs), 2025, http://dx.doi.org/10.48550/ARXIV.2503.05617.

[34] S. Nielles-Vallespin, Z. Khalique, P.F. Ferreira, R. de Silva, A.D. Scott, P. Kilner, L.-A. McGill, A. Giannakidis, P.D. Gatehouse, D. Ennis, E. Aliotta, M. Al-Khalil, P. Kellman, D. Mazilu, R.S. Balaban, D.N. Firmin, A.E. Arai, D.J. Pennell, Assessment of myocardial microstructural dynamics by In Vivo diffusion tensor cardiac magnetic resonance, J. Am. Coll. Cardiol. 69 (6) (2017) 661–676, http://dx.doi.org/10.1016/j.jacc.2016.11.051.

[35] P. Hauseux, J.S. Hale, S. Cotin, S.P.A. Bordas, Quantifying the uncertainty in a hyperelastic soft tissue model with stochastic parameters, Appl. Math. Model. 62 (2018) 86–102, http://dx.doi.org/10.1016/j.apm.2018.04.021.

[36] D. Ozturk, S. Kotha, S. Ghosh, An uncertainty quantification framework for multiscale parametrically homogenized constitutive models (PHCMs) of polycrystalline ti alloys, J. Mech. Phys. Solids 148 (2021) 104294, http://dx.doi.org/10.1016/j.jmps.2021.104294.

[37] A. Aggarwal, B.S. Jensen, S. Pant, C.-H. Lee, Strain energy density as a Gaussian process and its utilization in stochastic finite element analysis: Application to planar soft tissues, Comput. Methods Appl. Mech. Engrg. 404 (2023) 115812, http://dx.doi.org/10.1016/j.cma.2022.115812.

[38] A. Peshave, F. Pierron, P. Lava, D. Moens, D. Vandepitte, Practical uncertainty quantification guidelines for DIC-Based numerical model validation, Exp. Tech. (2024) http://dx.doi.org/10.1007/s40799-024-00758-1.

[39] D. Anton, J.-A. Tröger, H. Wessels, U. Römer, A. Henkes, S. Hartmann, Deterministic and statistical calibration of constitutive models from full-field data with parametric physics-informed neural networks, 2024, http://dx.doi.org/10.48550/ARXIV.2405.18311.

[40] V. Taç, M.K. Rausch, I. Bilionis, F. Sahli Costabal, A.B. Tepole, Generative hyperelasticity with physics-informed probabilistic diffusion fields, Eng. Comput. 41 (1) (2024) 51–69, http://dx.doi.org/10.1007/s00366-024-01984-2.

[41] K. Linka, G.A. Holzapfel, E. Kuhl, Discovering uncertainty: Bayesian constitutive artificial neural networks, Comput. Methods Appl. Mech. Engrg. 433 (2025) 117517, http://dx.doi.org/10.1016/j.cma.2024.117517.

[42] K.D. Costa, J.W. Holmes, A.D. Mcculloch, Modelling cardiac mechanical properties in three dimensions, Philos. Trans. R. Soc. Lond. Ser. A Math. Phys. Eng. Sci. 359 (1783) (2001) 1233–1250, http://dx.doi.org/10.1098/rsta.2001.0828.

[43] N. Laita, M.Á. Martínez, M. Doblaré, E. Peña, On the myocardium modeling under multimodal deformations: a comparison between costa's, Holzapfel and Ogden's formulations, Meccanica (2025) http://dx.doi.org/10.1007/s11012-025-01959-7.

[44] R. Avazmohammadi, J.S. Soares, D.S. Li, S.S. Raut, R.C. Gorman, M.S. Sacks, A contemporary look at biomechanical models of myocardium, Annu. Rev. Biomed. Eng. 21 (2019) 417–442, http://dx.doi.org/10.1146/annurev-bioeng-062117-121129.

[45] X. Navy, Z. Sheng, K. Kim, J.M. Cormack, Three-dimensional tissue strain measurement using a Row–Column array during biaxial testing of excised ventricular porcine myocardium, Ultrasound Med. Biol. 51 (9) (2025) 1622–1626, http://dx.doi.org/10.1016/j.ultrasmedbio.2025.05.007.

[46] J.B. Estrada, C.M. Luetkemeyer, U.M. Scheven, E.M. Arruda, MR-u: Material characterization using 3D displacement-encoded magnetic resonance and the virtual fields method, Exp. Mech. 60 (7) (2020) 907–924, http://dx.doi.org/10.1007/s11340-020-00595-4.

[47] S. Davis, A. Karali, T. Balcaen, J. Zekonyte, M. Pétré, M. Roldo, G. Kerckhofs, G. Blunn, Comparison of two contrast-enhancing staining agents for use in X-ray imaging and digital volume correlation measurements across the cartilage-bone interface, J. Mech. Behav. Biomed. Mater. 152 (2024) 106414, http://dx.doi.org/10.1016/j.jmbbm.2024.106414.

[48] R. Alberini, A. Spagnoli, M.J. Sadeghinia, B. Skallerud, M. Terzano, G.A. Holzapfel, Second harmonic generation microscopy, biaxial mechanical tests and fiber dispersion models in human skin biomechanics, Acta Biomater. 185 (2024) 266–280, http://dx.doi.org/10.1016/j.actbio.2024.07.026.

[49] A. Maes, C. Pestiaux, A. Marino, T. Balcaen, L. Leyssens, S. Vangrunderbeeck, G. Pyka, W.M. De Borggraeve, L. Bertrand, C. Beauloye, S. Horman, M. Wevers, G. Kerckhofs, Cryogenic contrast-enhanced microCT enables nondestructive 3D quantitative histopathology of soft biological tissues, Nat. Commun. 13 (1) (2022) http://dx.doi.org/10.1038/s41467-022-34048-4.

[50] M. Planck, Vorlesungen über Thermodynamik, von dr. Max Planck, Veit & Comp., 1897.

[51] B.D. Coleman, W. Noll, On the thermostatics of continuous media, Arch. Ration. Mech. Anal. 4 (1) (1959) 97–128, http://dx.doi.org/10.1007/BF00281381.

[52] M. Peirlinck, J.A. Hurtado, M.K. Rausch, A.B. Tepole, E. Kuhl, A universal material model subroutine for soft matter systems, Eng. Comput. (2024) http://dx.doi.org/10.1007/s00366-024-02031-w.

[53] R.V. Thorat, M. Anas, R. Nayek, S. Chatterjee, System identification and reliability assessment of hyperelastic materials via an efficient sparsity-promoting variational Bayesian approach, Probab. Eng. Mech. 80 (2025) 103763, http://dx.doi.org/10.1016/j.probengmech.2025.103763.

[54] M. Peirlinck, F. Sahli Costabal, K.L. Sack, J.S. Choy, G.S. Kassab, J.M. Guccione, M. De Beule, P. Segers, E. Kuhl, Using machine learning to characterize heart failure across the scales, Biomech. Model. Mechanobiol. 18 (6) (2019) 1987–2001, http://dx.doi.org/10.1007/s10237-019-01190-w.

[55] F. Rodrigues, Scaling Bayesian inference of mixed multinomial logit models to large datasets, Transp. Res. B 158 (2022) http://dx.doi.org/10.1016/j.trb.2022.01.005.

[56] S. Kullback, Information Theory and Statistics, Dover Publications, New York, 1968.

[57] J.A. Cover T., Information Theory and Statistics, Wiley-Interscience, 1968.

[58] G. Parisi, Statistical Field Theory, Addison-Wesley Pub. Co., Redwood City, CA, 1988.

[59] G. Consonni, J. Marin, Mean-field variational approximate Bayesian inference for latent variable models, Comput. Statist. Data Anal. 52 (2007) http://dx.doi.org/10.1016/j.csda.2006.10.028.

[60] D. Phan, N. Pradhan, M. Jankowiak, Composable effects for flexible and accelerated probabilistic programming in NumPyro, 2019, http://dx.doi.org/10.48550/arXiv.1912.11554.

[61] D.P. Kingma, J. Ba, Adam: A method for stochastic optimization, 2017.

[62] D.P. Kingma, M. Welling, Auto-Encoding variational Bayes, 2013, http://dx.doi.org/10.48550/ARXIV.1312.6114.

[63] H. Lombaert, J. Peyrat, P. Croisille, S. Rapacchi, L. Fanton, F. Cheriet, P. Clarysse, I. Magnin, H. Delingette, N. Ayache, Human Atlas of the cardiac fiber architecture: Study on a healthy population, IEEE Trans. Med. Imaging 31 (7) (2012) 1436–1447, http://dx.doi.org/10.1109/tmi.2012.2192743.

[64] D.S.S. Corp., Abaqus Analysis User's guide, Dassault Systèmes Simulia Corp., Providence, RI, USA, 2025.

[65] P.J. Flory, Thermodynamic relations for high elastic materials, Trans. Faraday Soc. 57 (1961) 829, http://dx.doi.org/10.1039/tf9615700829.

[66] A.J.M. Spencer, Constitutive theory for strongly anisotropic solids, in: Continuum Theory of the Mechanics of Fibre-Reinforced Composites, Springer Vienna, 1984, pp. 1–32, http://dx.doi.org/10.1007/978-3-7091-4336-0_1.

[67] A. Menzel, Modelling of anisotropic growth in biological tissues: A new approach and computational aspects, Biomech. Model. Mechanobiol. 3 (3) (2004) 147–171, http://dx.doi.org/10.1007/s10237-004-0047-6.

[68] W.H. Wittrick, A generalization of macaulay's method with applications in structural mechanics, AIAA J. 3 (2) (1965) 326–330, http://dx.doi.org/10.2514/3.2849.

[69] P. Wriggers, J. Schröder, F. Auricchio, Finite element formulations for large strain anisotropic material with inextensible fibers, Adv. Model. Simul. Eng. Sci. 3 (1) (2016) 25, http://dx.doi.org/10.1186/s40323-016-0079-3.

[70] E. McEvoy, G.A. Holzapfel, P. McGarry, Compressibility and anisotropy of the ventricular myocardium: Experimental analysis and microstructural modeling, J. Biomech. Eng. 140 (8) (2018) http://dx.doi.org/10.1115/1.4039947.

[71] F.C. Yin, C.C. Chan, R.M. Judd, Compressibility of perfused passive myocardium, Am. J. Physiol.-Heart Circ. Physiol. 271 (5) (1996) H1864–H1870, http://dx.doi.org/10.1152/ajpheart.1996.271.5.H1864.

[72] B. Rahmani, F. Mortazavi, I. Villemure, M. Levesque, A new approach to inverse identification of mechanical properties of composite materials: Regularized model updating, Compos. Struct. 105 (2013) 116–125, http://dx.doi.org/10.1016/j.compstruct.2013.04.025.

[73] R. Avazmohammadi, D.S. Li, T. Leahy, E. Shih, J.S. Soares, J.H. Gorman, R.C. Gorman, M.S. Sacks, An integrated inverse model-experimental approach to determine soft tissue three-dimensional constitutive parameters: application to post-infarcted myocardium, Biomech. Model. Mechanobiol. 17 (1) (2018) 31–53, http://dx.doi.org/10.1007/s10237-017-0943-1.

[74] H. Gao, W.G. Li, L. Cai, C. Berry, X.Y. Luo, Parameter estimation in a Holzapfel–Ogden law for healthy myocardium, J. Engrg. Math. (2015) http://dx.doi.org/10.1007/s10665-014-9740-3.

[75] A. Palit, S.K. Bhudia, T.N. Arvanitis, G.A. Turley, M.A. Williams, In vivo estimation of passive biomechanical properties of human myocardium, Med. Biol. Eng. Comput. (2018) http://dx.doi.org/10.1007/s11517-017-1768-x.

[76] A. Lazarus, D. Dalton, D. Husmeier, H. Gao, Sensitivity analysis and inverse uncertainty quantification for the left ventricular passive mechanics, Biomech. Model. Mechanobiol. (2022) http://dx.doi.org/10.1007/s10237-022-01571-8.

[77] G. Balaban, M.S. Alnæs, J. Sundnes, M.E. Rognes, Adjoint multi-start-based estimation of cardiac hyperelastic material parameters using shear data, Biomech. Model. Mechanobiol. (2016) http://dx.doi.org/10.1007/s10237-016-0780-7.

[78] Y. Ge, D. Husmeier, A. Rabbani, H. Gao, Advanced statistical inference of myocardial stiffness: A time series Gaussian process approach of emulating cardiac mechanics for real-time clinical decision support, 2025, http://dx.doi.org/10.1016/j.compbiomed.2024.109381.

[79] A. Jafari, K. Vlachas, E. Chatzi, J.F. Unger, A Bayesian framework for constitutive model identification via use of full field measurements, with application to heterogeneous materials, Comput. Methods Appl. Mech. Engrg. 433 (2025) 117489, http://dx.doi.org/10.1016/j.cma.2024.117489.

[80] K. Linka, E. Kuhl, A new family of constitutive artificial neural networks towards automated model discovery, Comput. Methods Appl. Mech. Engrg. 403 (2023) 115731, http://dx.doi.org/10.1016/j.cma.2022.115731.

[81] A. Marek, F.M. Davis, M. Rossi, F. Pierron, Extension of the sensitivity-based virtual fields to large deformation anisotropic plasticity, Int. J. Mater. Form 12 (3) (2019) 457–476, http://dx.doi.org/10.1007/s12289-018-1428-1.

[82] S. Ghouli, M. Flaschel, S. Kumar, L. De Lorenzis, A topology optimisation framework to design test specimens for one-shot identification or discovery of material models, J. Mech. Phys. Solids 203 (2025) 106210, http://dx.doi.org/10.1016/j.jmps.2025.106210.

[83] K.L. Chaurasiya, S. Dutta, S. Kumar, A. Joshi, Hetero-EUCLID: Interpretable model discovery for heterogeneous hyperelastic materials using stress-unsupervised learning, 2025, http://dx.doi.org/10.48550/ARXIV.2509.11784.